



Thermal imaging-based state estimation of a Stefan problem with application to cell thawing

Prakrit Srisuma^{a,b,c}, Ajinkya Pandit^b, Qihang Zhang^d, Moo Sun Hong^b, Janaka Gamekkanda^b, Fabio Fachin^e, Nathan Moore^e, Dragan Djordjevic^e, Michael Schwaerzler^e, Tolutola Oyetunde^e, Wenlong Tang^e, Allan S. Myerson^b, George Barbastathis^{a,c}, Richard D. Braatz^{b,c,*}

^a Department of Mechanical Engineering, Massachusetts Institute of Technology, Cambridge, MA 02139, USA

^b Department of Chemical Engineering, Massachusetts Institute of Technology, Cambridge, MA 02139, USA

^c Center for Computational Science and Engineering, Massachusetts Institute of Technology, Cambridge, MA 02139, USA

^d Department of Electrical Engineering and Computer Science, Massachusetts Institute of Technology, Cambridge, MA 02139, USA

^e Takeda Development Center Americas, Inc., Cambridge, MA 02139, USA

ARTICLE INFO

Keywords:

Stefan problems
Finite differences
Thermal imaging
Observer design
Cell thawing
Cell therapy

ABSTRACT

The Stefan problem describes the evolution of the interface between two phases of a material undergoing phase change. Its formulation has been applied to model and solve a wide range of science and engineering problems across industries. This article describes observer design of a Stefan problem that arises in cell therapy in which frozen cells need to be thawed before injection. The dynamic model is simulated via a finite difference scheme with the method of lines solved over a moving grid. A Luenberger observer is designed based on the continuous-time moving-boundary moving-grid equations and information from real-time thermal imaging. Simulation and experimental results show that the integrated numerical model and observer can precisely predict the spatiotemporal evolution of thawing with errors of 1%–2% throughout the cell thawing process despite sensor noise, offering a reliable approach for state estimation and monitoring of cell thawing.

1. Introduction

The classical Stefan problem is a heat transfer problem that describes the evolution of a moving interface in a freezing or melting process (Carslaw and Jaeger, 1959; Bird et al., 2002). The one-phase Stefan problem assumes the temperature of either liquid or solid to be constant at the melting/freezing point, whereas the two-phase Stefan problem considers temperature variations in both phases (Friedman and Kinderlehrer, 1975). The Stefan problem has been explored for a variety of boundary conditions, dimensions, coordinate systems, and other relevant assumptions (Carslaw and Jaeger, 1959; Meyer, 1971; Kar and Mazumder, 1994).

The Stefan problem arises in industrial and natural systems, e.g., casting (Kar and Mazumder, 1994), polymorphous materials formation (Tao, 1979), alloy formation (Brosa Planella et al., 2019, 2021), glaciation (Mikova et al., 2017), and phase change materials (Brezina et al., 2018). Stefan problems are also encountered in various biomedical scenarios including freezing and thawing of biological tissue during cryosurgery (Rubinsky and Shitzer, 1976; Rabin and Shitzer, 1995, 1997) and during cryopreservation (Dalwadi et al., 2020).

Many analytical and numerical techniques have been proposed for various types of Stefan problems. Exact analytical solutions to some specific Stefan problems have been derived for both one-phase (Bollati and Tarzia, 2018) and two-phase systems (McCord et al., 2016; Khalid et al., 2019). The analytical solutions typically involve Bessel functions, the error function, and/or infinite series. Numerical techniques have been developed for handling more general Stefan problems. Finite difference, volume, and element methods have been implemented on one- and two-phase Stefan problems (Meyer, 1971; Sartoretto and Spigler, 1990; Kutluay et al., 1997; Popov et al., 2005; Savović and Caldwell, 2009; Mitchell and Vynnycky, 2014; Karablenli et al., 2016; Kurbatova and Ermolaeva, 2019; Gusev et al., 2021).

State estimation and/or control of Stefan problems have also been investigated, including an observer-based backstepping-based control design for the one-phase Stefan problem (Koga et al., 2019), a full-state feedback control design for the two-phase Stefan problem for the continuous casting of steel (Petrus et al., 2010), and real-time estimation of an unmeasured heat flux at a boundary (Abdulla and Poggi, 2019). Applications to cell thawing, on the other hand, are

* Correspondence to: 77 Massachusetts Avenue, Cambridge, MA 02139, USA.
E-mail address: braatz@mit.edu (R.D. Braatz).

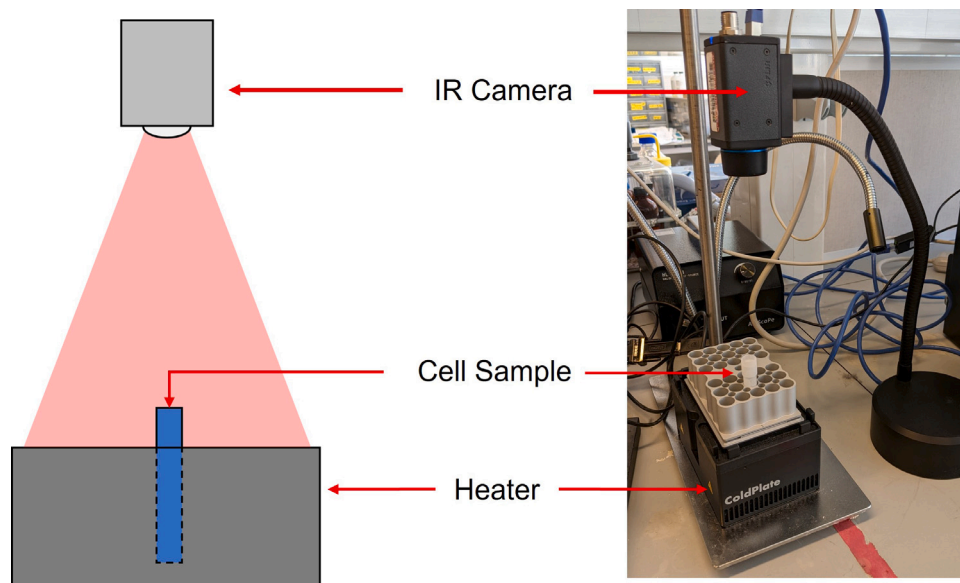


Fig. 1. Experimental system for cell thawing. A thermal imaging camera continuously measures the spatial temperature field during heating of a vial containing cells.

very limited. Optimization of freezing and thawing has been shown to improve the viability and quality of the resulting cells (Baboo et al., 2019; Hunt, 2019; Uhrig et al., 2022), and thus successful cryopreservation and cell thawing preceding injection are crucial in cell therapy (Hunt, 2019; Cottle et al., 2022). While some studies have analyzed and modeled cell thawing/freezing (Rubinsky and Shitzer, 1976; Rabin and Shitzer, 1995, 1997; Dalwadi et al., 2020), real-time state estimation and control based on a thawing/freezing model that simulates the solid–liquid interface have not been available.

This article presents a new approach for state estimation of Stefan problems and implements the approach to cell thawing. The Stefan problem is solved by a combination of the moving grid finite difference method and the numerical method of lines. A Luenberger observer is proposed for estimation of the spatially distributed states by using the information from real-time thermal imaging of the vial. The observer design is demonstrated in simulations and experiments.

This article is organized as follows. Section 2 describes the cell thawing system and associated mathematical model. Section 3 presents the numerical method for solving the Stefan problem. Section 4 describes the design and implementation of the Luenberger observer. Section 5 shows and discusses the simulation and experimental results obtained from implementing our model and observer in the real process. Finally, Section 6 summarizes the study and suggests some future directions.

2. Theoretical background and problem formulation

2.1. Cell thawing process

This article considers a cell thawing process used in cell therapy before cells are introduced to the patients. Prior to thawing, cryopreservation is used to temporarily store the cells. The cells are frozen at low temperature (around -80°C) to preserve their function, with the system being a single solid phase (consisting of cells, ice, and cryoprotection molecules) at its initial state. During thawing, energy is continuously supplied by a heating plate to thaw the material in each vial. When the mass fraction of frozen material decreases to about 5%, the vial is removed, and the cells are taken to the patient to be injected into the patient's body. The amount of frozen material left in the vial is specified so that all the vial contents are fluid by the time that the cells are injected into the patient; the small amount of frozen material keeps the aqueous solution from warming before injection.

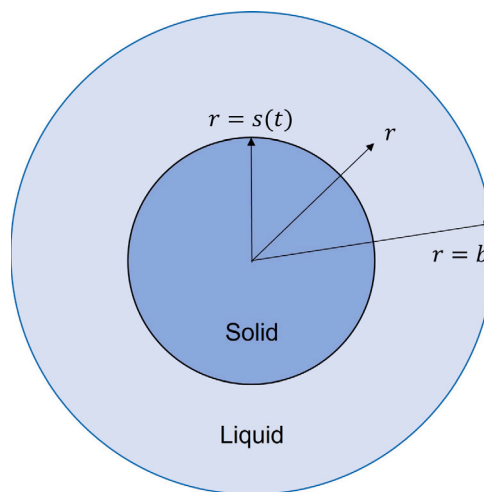


Fig. 2. Cell thawing with radial symmetry. The radial coordinate is r , the radius of the vial is b , and the radial position of the moving solid–liquid interface is $s(t)$.

Our experimental setup consists of a vial with the radius of 5 mm and height of 43 mm initially containing biological cells frozen in ice, a heating plate whose temperature is specified (e.g., fixed at 37°C), and a thermal imaging camera FLIR A35sc (FLIR, 2018) for monitoring the spatially varying temperature (Fig. 1). This setup combines commercial cell thawing equipment with a thermal imaging camera to provide real-time measurements for estimation and control.

Accurate prediction of the mass fraction of the solid can help achieve the best cell condition before these cells are injected, which directly benefits the patient. To track the mass fraction of the solid, a model for predicting the solid–liquid interface which directly relates to the volume of solid (and liquid) in the system is proposed. Considering the vial shape, the model is defined and formulated in cylindrical coordinates (r, θ, z) . As heat flow is primarily in the radial direction, the Stefan problem can be simplified to be in the radial dimension (Fig. 2).

2.2. Energy conservation

The energy conservation equation can be written as (Bird et al., 2002)

$$\rho C_p \frac{DT}{Dt} = -(\nabla \cdot \mathbf{q}) - \left(\frac{\partial \ln \rho}{\partial \ln T} \right)_p \frac{Dp}{Dt} - (\boldsymbol{\tau} : \nabla \mathbf{v}), \quad (1)$$

where T is the temperature, p is the pressure, \mathbf{q} is the heat flux governed by Fourier's law of heat conduction, \mathbf{v} is the velocity, $\boldsymbol{\tau}$ is the shear stress, t is time, ρ is the density, and C_p is the heat capacity. In cell thawing/freezing modeling, heat conduction is considered dominant compared to other heat transfer modes (Dalwadi et al., 2020; Hayashi et al., 2022). In our system, heat transfer can be omitted in the θ direction due to the vial being radially symmetric and in the z direction due to the low surface area of the bottom of the vial relative to the sides. Furthermore, the viscous dissipation term $-(\boldsymbol{\tau} : \nabla \mathbf{v})$ is much smaller than the other terms and can be neglected. In addition, the cells are relatively small compared with the length scales of the vial and create negligible biochemical reactions at the operating conditions, and so do not influence any phenomena in the system. Lastly, the liquid and solid have nearly constant thermal properties. By incorporating all these assumptions and substituting Fourier's law of heat conduction into (1), we obtain

$$\frac{1}{\alpha} \frac{\partial T}{\partial t} = \frac{\partial^2 T}{\partial r^2} + \frac{1}{r} \frac{\partial T}{\partial r}, \quad (2)$$

where $\alpha = k/(\rho C_p)$ denotes the thermal diffusivity, and k is the thermal conductivity. The subscripts 1 and 2 denote the solid and liquid phases, respectively. Hence, the governing equations for the solid region ($0 < r < s$) and liquid region ($s < r < b$) are

$$\frac{1}{\alpha_1} \frac{\partial T_1}{\partial t} = \frac{\partial^2 T_1}{\partial r^2} + \frac{1}{r} \frac{\partial T_1}{\partial r}, \quad (3)$$

$$\frac{1}{\alpha_2} \frac{\partial T_2}{\partial t} = \frac{\partial^2 T_2}{\partial r^2} + \frac{1}{r} \frac{\partial T_2}{\partial r}. \quad (4)$$

Define the times when thawing starts and completes as t_s and t_l , respectively. In a thawing problem where the initial state is pure solid, the solid domain exists when $t < t_l$, while the liquid domain exists when $t > t_s$. For $t_s < t < t_l$, both phases are present.

2.3. Boundary conditions

This section describes the boundary conditions for the model of the cell thawing system.

2.3.1. Outer boundary condition

The outer boundary of the vial, which is heated by the heating plate, satisfies the Robin boundary condition

$$\begin{cases} k_1 \frac{\partial T_1}{\partial r} = U(T_0 - T_1) & \text{for } t \leq t_s, \\ k_2 \frac{\partial T_2}{\partial r} = U(T_0 - T_2) & \text{for } t > t_s, \end{cases} \quad (5)$$

at $r = b$, where T_0 is the fixed heater temperature, and U is the overall heat transfer coefficient which takes into account the heat transfer resistance due to the cell vial thickness and the air gap between the cell vial and the heater. The heat transfer coefficient depends on multiple factors, including the unknown small gap between the outer wall of the vial and the heating plate, and is estimated from experimental data.

2.3.2. Symmetry condition

Symmetry of a cylinder implies the boundary condition

$$\begin{cases} \frac{\partial T_1}{\partial r} = 0 & \text{for } t < t_l, \\ \frac{\partial T_2}{\partial r} = 0 & \text{for } t \geq t_l, \end{cases} \quad (6)$$

at $r = 0$.

2.3.3. Stefan conditions

When $t_s < t < t_l$, heat transfer associated with thawing at the moving solid–liquid interface $r = s$ is described by the Stefan conditions

$$T_1 = T_2 = T_m, \quad (7)$$

$$\rho \Delta H_f \frac{ds}{dt} = k_1 \frac{\partial T_1}{\partial r} - k_2 \frac{\partial T_2}{\partial r}, \quad (8)$$

where ΔH_f is the latent heat of fusion, and T_m is the melting point. The first condition requires the temperature at the interface s to be T_m . The second condition is the energy balance associated with thawing at the moving interface. For the density ρ , past publications used the density of the solid (McCord et al., 2016), the density of the liquid (Mitchell and Vynnycky, 2014), or assumed that both phases have the same density (Šarler, 1995). The solid and liquid densities are not largely different, so any of these densities gives similar results. In our case, it is more convenient to use the density of the solid (ρ_1) because the equations are nondimensionalized with respect to the solid phase (Section 2.4).

2.4. Dimensionless quantities and equations

In transport phenomena, it is common to solve model equations in dimensionless form to minimize the number of parameters in the final problem formulation. A technique of nondimensionalization used in this work is appropriate for moving grids, i.e., the space between each grid point is varied with respect to the moving interface. This technique has been applied in pharmaceutical process modeling (Mesbah et al., 2014), and its concept is similar to the variable space grid method that has been used to solve some one-phase Stefan problems (Kutluay et al., 1997; Savović and Caldwell, 2009; Karabeni et al., 2016). An alternative nondimensionalization technique which is more common and produces fixed grids is given and discussed in Appendix A.

For two-phase problems, define the dimensionless variables and constants

$$R_1 = \frac{r}{s}, \quad (9)$$

$$R_2 = \frac{r-s}{b-s}, \quad (10)$$

$$\tau = \frac{\alpha_1 t}{b^2}, \quad (11)$$

$$\Theta_1 = \frac{T_1 - T_m}{T_0 - T_m}, \quad (12)$$

$$\Theta_2 = \frac{T_2 - T_m}{T_0 - T_m}, \quad (13)$$

$$S = \frac{s}{b}, \quad (14)$$

$$\text{Ste} = \frac{C_{p1}(T_0 - T_m)}{\Delta H_f}, \quad (15)$$

$$\alpha_0 = \frac{\alpha_2}{\alpha_1}, \quad (16)$$

$$k_0 = \frac{k_2}{k_1}, \quad (17)$$

$$U_0 = \frac{Ub}{k_2}, \quad (18)$$

where Ste is the Stefan number. We use R_1 and R_2 to denote the radial position within the solid and the radial position within the liquid, respectively. Both R_1 and R_2 depend on the radial position of the moving interface s , which results in moving grids when the equations are discretized. From (9), $R_1 = 0$ at the center $r = 0$, and $R_1 = 1$ at the solid–liquid interface $r = s$. Similarly, from (10), $R_2 = 0$ at the solid–liquid interface s , and $R_2 = 1$ at the outer boundary $r = b$. This type of nondimensionalization has several advantages which are discussed in Section 3.

With these dimensionless variables, applying the chain rule to all the derivative terms in (3) and (4) results in

$$\frac{\partial T_1}{\partial t} = \frac{\alpha_1(T_0 - T_m)}{b^2} \frac{\partial \Theta_1}{\partial \tau} - \frac{\alpha_1 R_1(T_0 - T_m)}{b^2 S} \frac{\partial \Theta_1}{\partial R_1} \frac{dS}{d\tau}, \quad (19)$$

$$\frac{\partial T_1}{\partial r} = \frac{T_0 - T_m}{bS} \frac{\partial \Theta_1}{\partial R_1}, \quad (20)$$

$$\frac{\partial^2 T_1}{\partial r^2} = \frac{T_0 - T_m}{b^2 S^2} \frac{\partial^2 \Theta_1}{\partial R_1^2}, \quad (21)$$

$$\frac{\partial T_2}{\partial r} = \frac{\alpha_1(T_0 - T_m)}{b^2} \frac{\partial \Theta_2}{\partial \tau} - \frac{\alpha_1(1 - R_2)(T_0 - T_m)}{b^2(1 - S)} \frac{\partial \Theta_2}{\partial R_2} \frac{dS}{d\tau}, \quad (22)$$

$$\frac{\partial T_2}{\partial r} = \frac{T_0 - T_m}{b(1 - S)} \frac{\partial \Theta_2}{\partial R_2}, \quad (23)$$

$$\frac{\partial^2 T_2}{\partial r^2} = \frac{T_0 - T_m}{b^2(1 - S)^2} \frac{\partial^2 \Theta_2}{\partial R_2^2}. \quad (24)$$

Substituting (19)–(24) into (3) and (4) results in the nondimensionalized partial differential equations (PDEs)

$$\frac{\partial \Theta_1}{\partial \tau} = \frac{1}{S^2} \frac{\partial^2 \Theta_1}{\partial R_1^2} + \frac{1}{S^2 R_1} \frac{\partial \Theta_1}{\partial R_1} + \frac{R_1}{S} \frac{dS}{d\tau} \frac{\partial \Theta_1}{\partial R_1}, \quad (25)$$

$$\begin{aligned} \frac{1}{\alpha_0} \frac{\partial \Theta_2}{\partial \tau} &= \frac{1}{(1 - S)^2} \frac{\partial^2 \Theta_2}{\partial R_2^2} + \frac{1}{(1 - S)(S + R_2(1 - S))} \frac{\partial \Theta_2}{\partial R_2} \\ &+ \frac{1 - R_2}{\alpha_0(1 - S)} \frac{dS}{d\tau} \frac{\partial \Theta_2}{\partial R_2}, \end{aligned} \quad (26)$$

where (25) is for the solid region ($0 < R_1 < 1$), and (26) is for the liquid region ($0 < R_2 < 1$). The Robin boundary condition is

$$\begin{cases} \frac{1}{S} \left(\frac{\partial \Theta_1}{\partial R_1} \right) = U_0 k_0 (1 - \Theta_1) & \text{for } \tau \leq \tau_s, \text{ at } R_1 = 1, \\ \frac{1}{1 - S} \left(\frac{\partial \Theta_2}{\partial R_2} \right) = U_0 (1 - \Theta_2) & \text{for } \tau > \tau_s, \text{ at } R_2 = 1, \end{cases} \quad (27)$$

where τ_s is the dimensionless time evaluated at t_s . For the symmetry condition,

$$\begin{cases} \frac{1}{S} \left(\frac{\partial \Theta_1}{\partial R_1} \right) = 0 & \text{for } \tau < \tau_l, \text{ at } R_1 = 0, \\ \frac{1}{1 - S} \left(\frac{\partial \Theta_2}{\partial R_2} \right) = 0 & \text{for } \tau \geq \tau_l, \text{ at } R_2 = 0, \end{cases} \quad (28)$$

where τ_l is the dimensionless time evaluated at t_l . The Stefan conditions at $R_1 = 1$ and $R_2 = 0$ are

$$\Theta_1 = \Theta_2 = 0, \quad (29)$$

$$\frac{1}{\text{Ste}} \frac{dS}{d\tau} = \frac{1}{S} \frac{\partial \Theta_1}{\partial R_1} - \frac{k_0}{1 - S} \frac{\partial \Theta_2}{\partial R_2}. \quad (30)$$

This transformation results in nonlinear PDEs.

An analytical solution for the temperature profiles for the two-phase Stefan problem in the finite cylindrical domain has been derived using the separation of variables (Khalid et al., 2019). The analytical solution is in the form of an infinite series involving transcendental equations (Carslaw and Jaeger, 1959; Khalid et al., 2019), and cannot be written as a closed-form expression.¹ A closed-form expression for the interface position $S(\tau)$ is not available, motivating the use of the numerical methods in the next section.

3. Numerical methods

To produce moving grids, the radial positions are defined as

$$R_1 = i\Delta R, \quad (31)$$

$$R_2 = j\Delta R, \quad (32)$$

where i and j are the integer indices for discretization, $\Delta R = 1/n$, and n is the number of grid points. From (9) and (31), $i = 0$ and $R_1 = 0$ at the center $r = 0$, and $i = n$ and $R_1 = 1$ at the solid–liquid interface

$r = s$, respectively. Similarly, (10) and (32) imply that $j = 0$ and $R_2 = 0$ at the solid–liquid interface $r = s$, and $j = n$ and $R_2 = 1$ at the outer boundary $r = b$.

The transformation in Section 2.4 and discretization explained above allow grid size to be varied with the position of a moving interface to capture the system behavior accurately. As the solid–liquid interface moves, the size of grids in the solid phase decreases, while that in the liquid phase increases (Figs. 3 and 4). In addition, the number of grid points in each phase is constant irrespective of the interface position. This property ensures that the number of grids is always sufficient at any stage of thawing. Moreover, state estimation and process control are simplified because the number of states is constant in both regions all the time.

Neither of the aforementioned properties can be achieved if the problem is solved in a fixed grid domain, which makes the moving grid approach superior to the typical fixed grid approach in nearly all aspects. The only drawback of the moving grid approach is that it is significantly more complicated in terms of mathematical derivation and computation (See Appendix B for comparison).

In this work, the numerical method of lines (Schuesser, 1991) is applied for discretization. This technique discretizes the spatial derivatives only, converting each PDE into a system of ordinary differential equations (ODEs). The resulting ODEs can be solved by available solvers such as ode45 and ode15s in MATLAB. These ODE solvers employ highly efficient adaptive time stepping procedures, which is computationally efficient, especially when the time step needs to be small to achieve numerical accuracy for some of the time.

Discretizing the governing PDEs (25) and (26) using the central difference (second-order accurate) approximation and the numerical method of lines results in

$$\begin{aligned} \frac{d(\Theta_1)_i}{d\tau} &= \frac{1}{S^2} \left(\frac{(\Theta_1)_{i+1} - 2(\Theta_1)_i + (\Theta_1)_{i-1}}{(\Delta R)^2} \right) \\ &+ \frac{1}{S^2(i\Delta R)} \left(\frac{(\Theta_1)_{i+1} - (\Theta_1)_{i-1}}{2\Delta R} \right) \\ &+ \frac{i\Delta R}{S} \left(\frac{(\Theta_1)_{i+1} - (\Theta_1)_{i-1}}{2\Delta R} \right) \left(\frac{dS}{d\tau} \right), \end{aligned} \quad (33)$$

$$\begin{aligned} \frac{d(\Theta_2)_j}{d\tau} &= \frac{\alpha_0}{(1 - S)^2} \left(\frac{(\Theta_2)_{j+1} - 2(\Theta_2)_j + (\Theta_2)_{j-1}}{(\Delta R)^2} \right) \\ &+ \frac{\alpha_0}{(1 - S)(S + j\Delta R(1 - S))} \left(\frac{(\Theta_2)_{j+1} - (\Theta_2)_{j-1}}{2\Delta R} \right) \\ &+ \frac{1 - j\Delta R}{1 - S} \left(\frac{(\Theta_2)_{j+1} - (\Theta_2)_{j-1}}{2\Delta R} \right) \left(\frac{dS}{d\tau} \right). \end{aligned} \quad (34)$$

The Robin boundary condition can be treated by applying the central difference scheme

$$\begin{cases} \frac{1}{S} \left(\frac{(\Theta_1)_{n+1} - (\Theta_1)_{n-1}}{2\Delta R} \right) = U_0 k_0 (1 - (\Theta_1)_n) & \text{for } \tau \leq \tau_s, \\ \frac{1}{1 - S} \left(\frac{(\Theta_2)_{n+1} - (\Theta_2)_{n-1}}{2\Delta R} \right) = U_0 (1 - (\Theta_2)_n) & \text{for } \tau > \tau_s. \end{cases} \quad (35)$$

The temperatures at $i, j = n + 1$ are not in the domain but can be eliminated by coupling (35) with the governing PDEs at $i, j = n$. Several techniques are available for treating the symmetry condition. One technique is to first apply L'Hôpital's rule to the governing PDEs at $R_1, R_2 = 0$ to eliminate the singularity, and then discretize the PDEs as usual, resulting in

$$\begin{cases} \frac{d(\Theta_1)_0}{d\tau} = \frac{4}{S^2} \left(\frac{(\Theta_1)_1 - (\Theta_1)_0}{(\Delta R)^2} \right) & \text{for } \tau < \tau_l, \\ \frac{d(\Theta_2)_0}{d\tau} = \frac{4\alpha_0}{(1 - S)^2} \left(\frac{(\Theta_2)_1 - (\Theta_2)_0}{(\Delta R)^2} \right) & \text{for } \tau \geq \tau_l. \end{cases} \quad (36)$$

This technique, which has been applied in many diffusion problems (e.g., Crank (1975), Ford Versypt and Braatz (2014)), is second-order accurate at the singularity point $r = 0$. For the Stefan conditions, the

¹ A closed-form expression is a mathematical formula with a finite number of terms containing no limits, differentiations, or integrals.

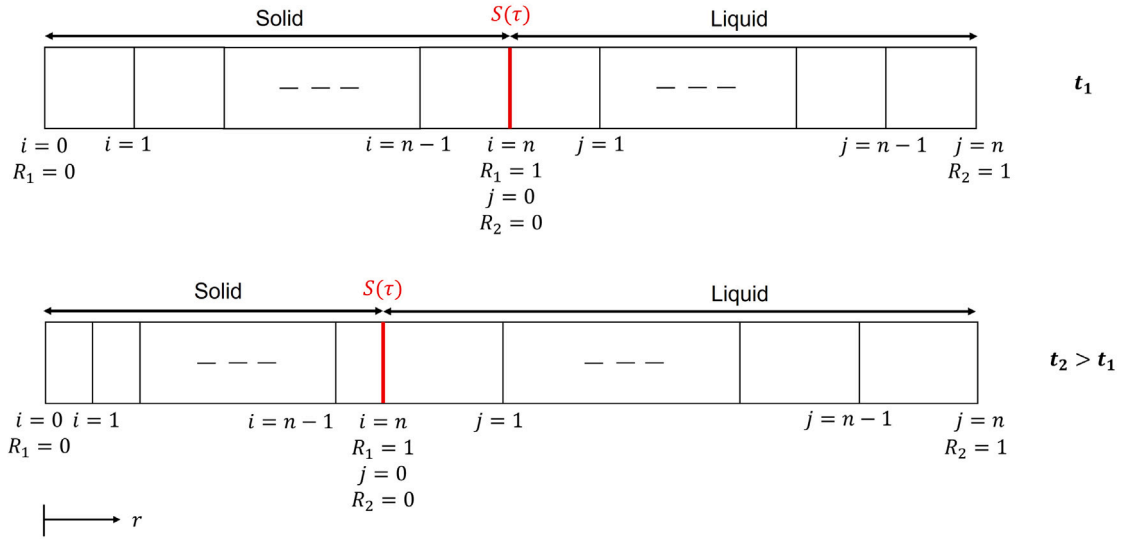


Fig. 3. Discretization of the moving grid domain.

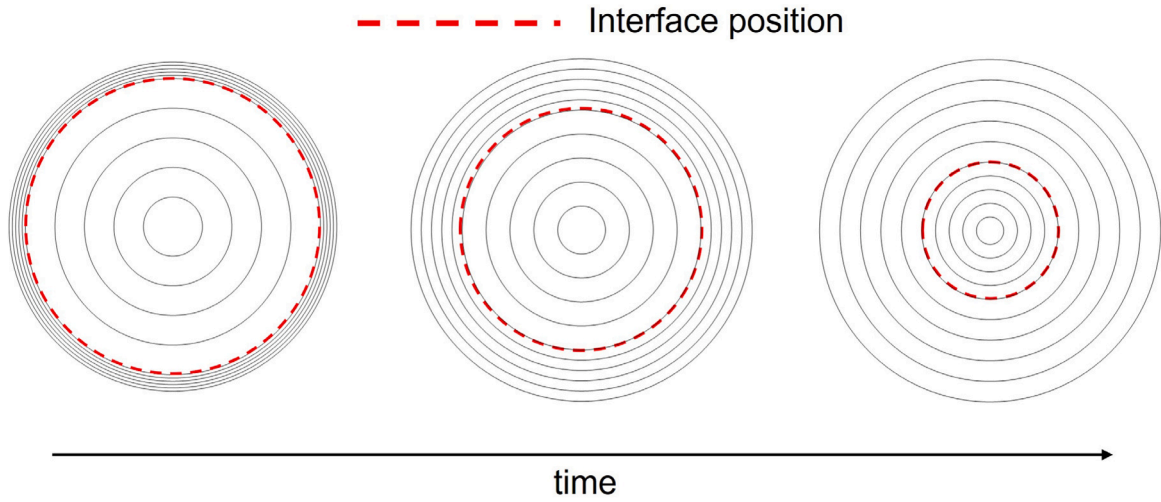


Fig. 4. Evolution of the solid-liquid interface in the moving grid domain.

second-order forward and backward difference schemes can be applied to the liquid and solid sides, respectively, which gives

$$(\Theta_1)_n = (\Theta_2)_0 = 0, \quad (37)$$

$$\frac{dS}{d\tau} = \frac{\text{Ste}}{S} \left(\frac{3(\Theta_1)_n}{2\Delta R} - \frac{2(\Theta_1)_{n-1}}{\Delta R} + \frac{(\Theta_1)_{n-2}}{2\Delta R} \right) - \frac{k_0 \text{Ste}}{1-S} \left(-\frac{3(\Theta_2)_0}{2\Delta R} + \frac{2(\Theta_2)_1}{\Delta R} - \frac{(\Theta_2)_2}{2\Delta R} \right). \quad (38)$$

During the thawing process ($\tau_s < \tau < \tau_l$), all the above equations can be simplified to

$$\frac{d(\Theta_1)_0}{d\tau} = f_1((\Theta_1)_0, (\Theta_1)_1, S) \quad \text{for } i = 0, \quad (39)$$

$$\frac{d(\Theta_1)_i}{d\tau} = f_2((\Theta_1)_{i-1}, (\Theta_1)_i, (\Theta_1)_{i+1}, S, \frac{dS}{d\tau}) \quad \text{for } i = 1, \dots, n-1, \quad (40)$$

$$\frac{d(\Theta_2)_j}{d\tau} = f_3((\Theta_2)_{j-1}, (\Theta_2)_j, (\Theta_2)_{j+1}, S, \frac{dS}{d\tau}) \quad \text{for } j = 1, \dots, n-1, \quad (41)$$

$$\frac{d(\Theta_2)_n}{d\tau} = f_4((\Theta_2)_{n-1}, (\Theta_2)_n, S) \quad \text{for } j = n, \quad (42)$$

$$\frac{dS}{d\tau} = f_5((\Theta_1)_{n-2}, (\Theta_1)_{n-1}, (\Theta_1)_n, (\Theta_2)_0, (\Theta_2)_1, (\Theta_2)_2, S), \quad (43)$$

where f_1, f_2, f_3, f_4 and f_5 are the nonlinear functions, and $(\Theta_1)_n = (\Theta_2)_0 = 0$. The state vector $\mathbf{x} \in \mathbb{R}^{2n+1}$ can be defined as

$$\mathbf{x} = \begin{bmatrix} \mathbf{x}_1 \\ \mathbf{x}_2 \\ x_3 \end{bmatrix}, \quad (44)$$

where $\mathbf{x}_1 \in \mathbb{R}^n$ collects the temperature profile of the solid $(\Theta_1)_i$ from $i = 0$ to $i = n-1$, $\mathbf{x}_2 \in \mathbb{R}^n$ collects the temperature profile of the liquid $(\Theta_2)_j$ from $j = 1$ to $j = n$, and x_3 is the interface position S . As a result, (39)–(43) can be written as

$$\frac{d\mathbf{x}_1}{d\tau} = \mathbf{F}_1(\mathbf{x}, \mathbf{u}), \quad (45)$$

$$\frac{d\mathbf{x}_2}{d\tau} = \mathbf{F}_2(\mathbf{x}, \mathbf{u}), \quad (46)$$

$$\frac{dx_3}{d\tau} = F_3(\mathbf{x}, \mathbf{u}), \quad (47)$$

where \mathbf{u} is the vector of manipulated variables (e.g., heater temperature) and $\mathbf{F}_1 \in \mathbb{R}^n$, $\mathbf{F}_2 \in \mathbb{R}^n$, $F_3 \in \mathbb{R}$ denote the nonlinear functions of \mathbf{x} and \mathbf{u} . For implementation, (45)–(47) can be integrated using ode15s in MATLAB.

4. State estimation

This section describes the design of a state observer (aka state estimator) for the moving grid two-phase Stefan problem and its application to (45)–(47) for state estimation and control of the cell thawing process.

4.1. Mathematical structure of the observer

Our primary aim of constructing an observer is to estimate the states in the moving grid model from the measurements. Well-known observers include the Luenberger observer, Kalman filter, high-gain observer, sliding-mode observer, and moving horizon estimator (Kalman, 1960; Luenberger, 1971; Wang and Gao, 2003; Kumar et al., 2013; Jang et al., 2014).

Detailed discussion and comparison of state observers for chemical processes can be found in Mohd Ali et al. (2015). Luenberger observers are computationally efficient for both linear and nonlinear processes, which has resulted in widespread use in various applications (Tarantino et al., 2000; Vries et al., 2007; Mohd Ali et al., 2015). Kalman filtering has been heavily investigated in the academic literature of varying degrees of computational complexity for both linear and nonlinear processes, but all require knowledge of the process and measurement covariance matrices (Kalman, 1960). That information is not available for cell thawing, and so the covariance matrices become additional degrees of freedom for observer design, resulting in many more degrees of freedom than a Luenberger observer. Moving horizon estimation, which is an optimization-based estimator, has a much higher on-line computational cost than the Luenberger observer, especially for nonlinear distributed parameter systems (Jang et al., 2014). An observer for cell thawing needs to be solvable within seconds (the entire cell thawing process is completed in a few minutes). These considerations motivate the use of a Luenberger observer for state estimation for cell thawing.

Applying the Luenberger observer to our moving grid model (45)–(47) results in

$$\frac{d\hat{x}_1}{d\tau} = F_1(\hat{x}, u) + L_1(\hat{y}_1 - y_1), \quad (48)$$

$$\frac{d\hat{x}_2}{d\tau} = F_2(\hat{x}, u) + L_2(\hat{y}_2 - y_2), \quad (49)$$

$$\frac{d\hat{x}_3}{d\tau} = F_3(\hat{x}, u) + L_3(\hat{y}_3 - y_3), \quad (50)$$

where $\hat{x}_1, \hat{x}_2, \hat{x}_3$ are the estimated states corresponding to x_1, x_2, x_3 ; L_1, L_2, L_3 are the Luenberger observer gains; y_1, y_2, y_3 are the measured outputs; and $\hat{y}_1, \hat{y}_2, \hat{y}_3$ are the estimated outputs. The temperature profiles and interface position are approximated from the data provided by the thermal imaging camera (Fig. 1), so the output vectors are

$$\hat{y}_1 = C_1 \hat{x}_1, \quad (51)$$

$$y_1 = C_1 x_1 + n_1, \quad (52)$$

$$\hat{y}_2 = C_2 \hat{x}_2, \quad (53)$$

$$y_2 = C_2 x_2 + n_2, \quad (54)$$

$$\hat{y}_3 = C_3 \hat{x}_3, \quad (55)$$

$$y_3 = C_3 x_3 + n_3, \quad (56)$$

where $C_1 = C_2 = I_n$; I_n is the $n \times n$ identity matrix; C_3 is 1; and $n_1 \in \mathbb{R}^n, n_2 \in \mathbb{R}^n, n_3 \in \mathbb{R}$ represent sensor noise.

The Luenberger observer is divided into three main parts: (48) estimates the temperature profile of the solid, (49) estimates the temperature profile of the liquid, and (50) estimates the interface position. This observer structure separates the states in three regions, each of which depends on a different set of parameters and measurement data, while respecting the coupling of the states in the moving grid model. The states of the observer in each region are updated by the

corresponding measurements. In addition, this structure simplifies the selection of the observer gains. The control stopping criterion for cell thawing is the specified fraction of frozen material at the end of the thawing, which is directly related to the interface position rather than the temperature profiles within the solid and liquid phases. As such, the estimation of the interface position $x_3 = S$ is of primary interest, with the estimation of the other states of lesser importance.

4.2. Observer design procedure

The observer gains are selected to trade off sensitivity to measurement noise with speed of convergence of the state estimates. In (48)–(50), the observer gains $L_1 \in \mathbb{R}^{n \times n}$ and $L_2 \in \mathbb{R}^{n \times n}$ correspond to the number of grid points, while L_3 is a real scalar for the one interface position. The measurement noise in the infrared sensor is not spatially dependent, which suggests a parameterization with one degree of freedom in each phase:

$$L_1 = L_1 I_n, \quad (57)$$

$$L_2 = L_2 I_n, \quad (58)$$

where L_1 and L_2 are real scalars. With this parameterization, each spatial domain has one design parameter.

Each observer gain (L_1, L_2 , and L_3) is selected to steer the states in the associated spatial domain in the first-principles model to the correct states given the measurement data. A higher gain results in faster convergence of the model states but increases the effects of measurement noise on the state estimates. The value of each gain is selected to converge the model states to the correct states as fast as possible without significantly polluting the state estimates by measurement noise.

In a linear, observable system, the Luenberger observer gain can be designed based on the eigenvalues of the closed-loop state equations (Luenberger, 1971). In our nonlinear model, the observer gains are designed in a two-step procedure. The first step relies entirely on the first-principles model developed in (45)–(56), whereas the second step takes the data/measurement obtained from the real system into account. For convenience, we denote the first step as *model-based design* and the latter as *data-based design*.

For the model-based design, the first-principles model and observer given by (45)–(56) are simulated to determine a range of observer gains that may have a practically reasonable convergence rate and filtering of measurement noise, without taking into account plant/model mismatch. After that step, the observer gains are refined by using the real data. For the data-based design, (52), (54), and (56) are replaced by the real measurement data, and the observer gains are varied. This step ensures that the design is based on the actual performance of the observer and tunes the observer gain to account for real measurement data and plant/model mismatch. The design and actual performance of the observer are shown in Section 5.

The model-based design allows for different models and noise profiles to be tested so that the resulting design can cover many possible scenarios, whereas the data-based design is primarily specific to the system where the real data are available. The former enables an initial observer design and performance assessment before the experimental system is set up. On the other hand, as the first-principles model is not perfect, and noise characteristics are not precisely known until the system is set up, the second step selects observer gains to account for that. The two-step approach to observer design saves time while providing an assurance of robustness in the final design.

5. Results and discussion

This section firstly describes the simulation results obtained from simulating the first-principles model in Section 3 and compares the results to the experimental data. Subsequently, the Luenberger observer

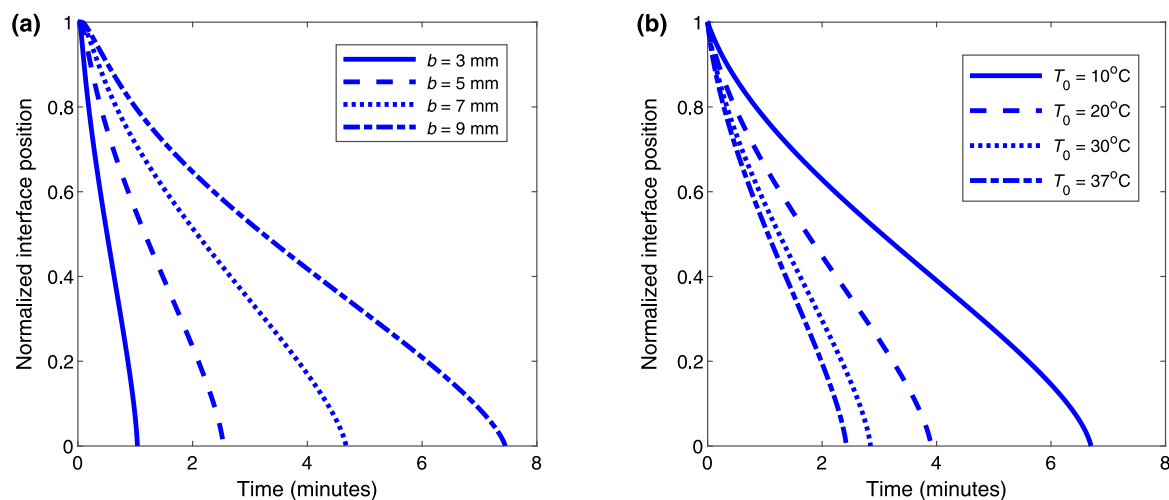


Fig. 5. Time evolution of the radial position of the solid-liquid interface predicted by the first-principles model for (a) four values of the vial radius with the heater temperature of 37°C and (b) four values of the heater temperature with the vial radius of 5 mm. The initial temperature of the solid phase is uniform at -80°C , and the initial temperature of the liquid phase is uniform at the melting point temperature of -2°C .

Table 1
Default parameters in the simulations.

Parameter	Value	Unit	Description
ρ_1	916	kg/m^3	Density of the solid
ρ_2	1000	kg/m^3	Density of the liquid
k_1	2.22	W/(m K)	Thermal conductivity of the solid
k_2	0.556	W/(m K)	Thermal conductivity of the liquid
C_{p1}	2.050	$\text{kJ/(kg }^{\circ}\text{C)}$	Heat capacity of the solid
C_{p2}	4.204	$\text{kJ/(kg }^{\circ}\text{C)}$	Heat capacity of the liquid
ΔH_f	334	kJ/kg	Latent heat of fusion
U	850	$\text{W/(m}^2\text{ K)}$	Overall heat transfer coefficient
b	5	mm	Vial radius
T_0	37	$^{\circ}\text{C}$	Heater temperature
T_m	-2	$^{\circ}\text{C}$	Melting point
n	50	–	Number of grid points

design results derived following the procedure in Section 4 are presented. Finally, the results from implementing the complete model and observer to perform real-time state estimation and control of the cell thawing process are discussed. Table 1 lists the default parameters used in the simulations.

5.1. Simulation results and model validation

5.1.1. Simulation results

Figs. 5–7 show the solid-liquid interface position and temperature profiles predicted by the first-principles model (45)–(47). From Fig. 5, the position of the solid-liquid interface decreases linearly at the beginning, and that decrease becomes slower as the driving force for heat transfer, i.e., the temperature difference between the heater and the vial, is lower. At the end of the process, the interface position drops rapidly, which is consistent with the increasing surface-area-to-volume ratio of the solid core. The time for complete thawing ranges from 1 min to about 7 min, with an increase of a factor of seven for an increase in the vial radius of a factor of three (Fig. 5a). Increasing the heater temperature by 27°C reduces the thawing time by about a factor of three (Fig. 5b).

The model predictions are consistent with typical thawing times in the literature. Previous studies have suggested a thawing temperature of 37°C with thawing times of less than 5 min (Baboo et al., 2019; Hunt, 2019). A thawing time of about 3 min was experimentally observed for a vial size similar to our vial of radius 5 mm (Baboo et al., 2019).

For a vial of radius 5 mm and the standard heater temperature of 37°C, the temperature during thawing is nearly linear near the solid-liquid interface in the solid phase (Fig. 6a) and over the whole domain in the liquid phase (Fig. 6b). The spatial profile of the temperature in the solid deviates from linearity at its center ($R_1 = 0$), which is consistent with the radial symmetry condition. Once some of the heat has transferred to the center of the solid, the spatial profile retains a similar curved shape, eventually reaching the melting point once the solid core is sufficiently thin. The time scale of heat conduction in the liquid phase is about ten times slower than that of the solid phase (cf., Fig. 6ab).

In Fig. 7, the temperature of the solid increases from -80°C to the melting point of -2°C within half a minute, so the solid temperature profile is flat most of the time. The liquid temperature at the inner glass surface of the vial (5 mm) evolves from its melting point to about 30°C by the end of the thawing. The mesh spacing in Fig. 7 shows how the moving grid evolves during the simulation, i.e., the grid size in each domain varies as the interface position changes, with fine spatial resolution in the liquid phase near the start and in the solid phase near the end of the thawing.

5.1.2. Model validation

This section validates the first-principles model using the experimental data. To measure the temperature profile and interface position in each experiment, the thermal imaging camera was oriented to monitor the temperature from the top of the vial (Fig. 1). Some examples of the image data and relevant data analysis procedure are given in Appendix C.

Fig. 8 compares the value of the interface position predicted by the first-principles model initialized by the measured temperatures and interface position at time $t = 0$ with the measured interface position throughout the thawing. The prediction of the first-principles model deviates from the measured interface position by less than 0.05 (i.e., 5% of the vial radius) during the first 2 min but by more than 10% at later times when the interface position drops more rapidly. One cause of the deviation is that the first-principles model is based on heat transfer in one spatial dimension, but the actual thawing process occurs in three spatial dimensions. Another potential cause is that some movement of the frozen material could occur when most of the material is liquid. Such movement can enhance convective heat transfer and induce asymmetric effects. This deviation can be improved by using a well-designed observer (Section 5.3).

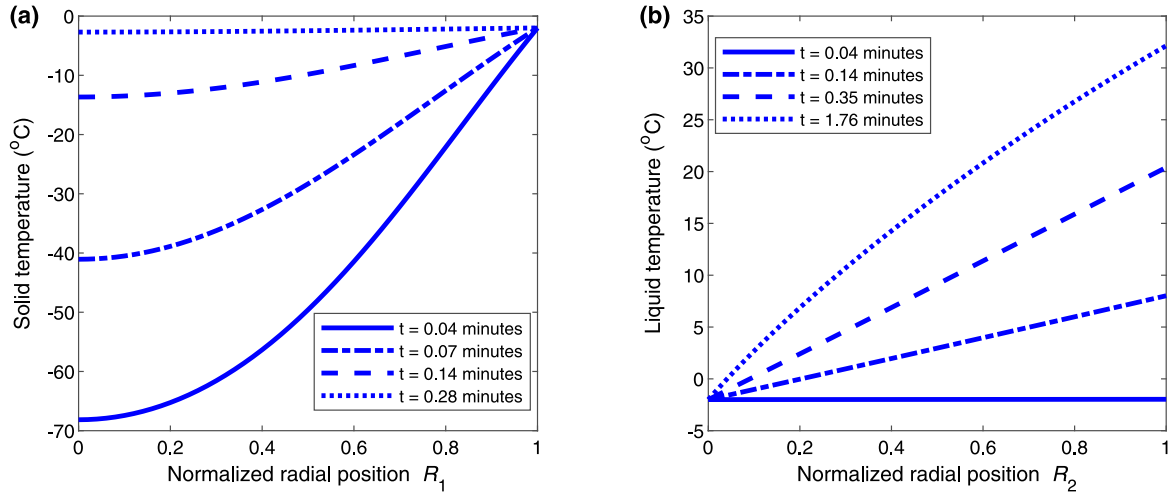


Fig. 6. Spatiotemporal evolution of the temperatures of the (a) solid and (b) liquid phases for the default vial radius (5 mm) and heater temperature (37°C). The initial temperature of the solid phase is uniform at -80°C , and the initial temperature of the liquid phase is uniform at the melting point temperature of -2°C . The normalized position is used to help visualize the plots easily.

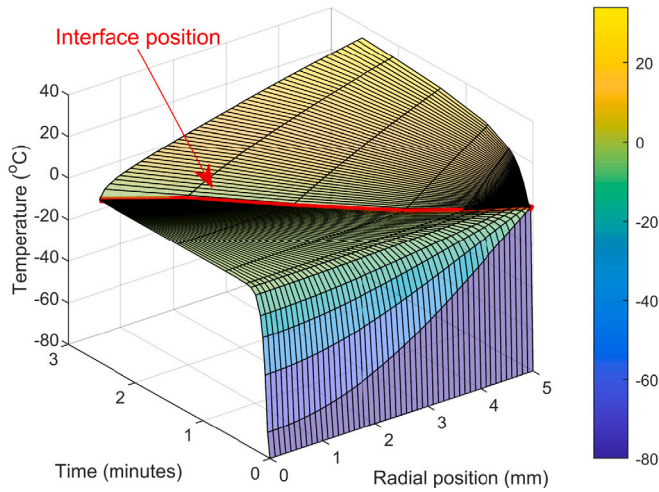


Fig. 7. Spatiotemporal evolution of the temperature of the solid and liquid phases in the original coordinates for a vial of radius 5 mm and the heater temperature of 37°C. The initial temperature of the solid phase is uniform at -80°C , and the initial temperature of the liquid phase is uniform at the melting point temperature of -2°C .

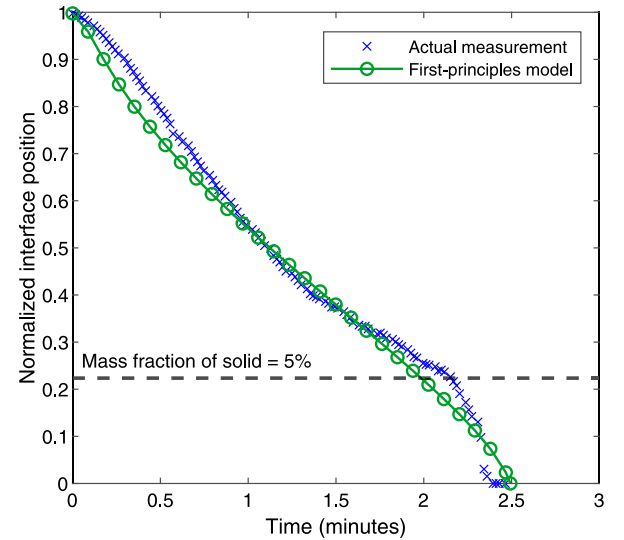


Fig. 8. Time evolution of the measured and predicted interface position for the vial radius of 5 mm and heater temperature of 37°C. The first-principles model is initialized by the measured initial temperatures and interface position.

5.2. Observer design

With the first-principles model established, the observer was designed following the procedure in Section 4.2. The observer has three gains: L_1 , L_2 , and L_3 . Since the objective of cell thawing estimation is to track the interface position, this section first focuses on the design of the associated observer gain L_3 . Then the section shows that values of the observer gains L_1 and L_2 do not significantly affect the interface tracking performance.

5.2.1. Observer gain selection

Noise-free model-based simulation results show that the proposed observer converges for a wide range of values of the observer gain L_3 for the solid–liquid interface (Fig. 9). The estimated interface position converges to the actual value in 30 s for values of the observer gain L_3 from -2 to -15 , and slowly for $L_3 = -1/2$.

Model-based simulation results with normally distributed measurement noise show similarly fast convergence of the estimated interface position for values of the observer gain L_3 from -2 to -15 and poor

convergence for $L_3 = -1/2$ (Fig. 10). For $L_3 = -2$, the estimated interface position is smooth and almost not polluted by noise (Fig. 10b). The estimate of the interface position is slightly noisy for $L_3 = -5$ but still provides a good estimate (Fig. 10c), implying that the gain should not be increased much further. When the observer gain is too high, the estimated interface position is noisy and does not give a good estimate of the state (Fig. 10d). These model-based results suggest that the optimal observer gain should be within the range of -2 to -5 , with the final value decided by application to the experimental data.

When the observer is applied to experimental data, the estimated interface position reaches the measured value within 30 s for four values of the observer gain L_3 between -2 and -5 (Fig. 11). The observer poorly tracks the interface position between 0.5 to 1.5 min and after 2 min with the observer gain $L_3 = -2$ and -3 (Fig. 11ab), indicating the gain is too small. The convergence is improved for L_3 of -4 and -5 , respectively (Fig. 11cd). For the observer gain $L_3 = -5$, the estimated interface position converges to the measured value throughout the process with slight deviation during the last few seconds where the interface drops rapidly (Fig. 11d). This small deviation is

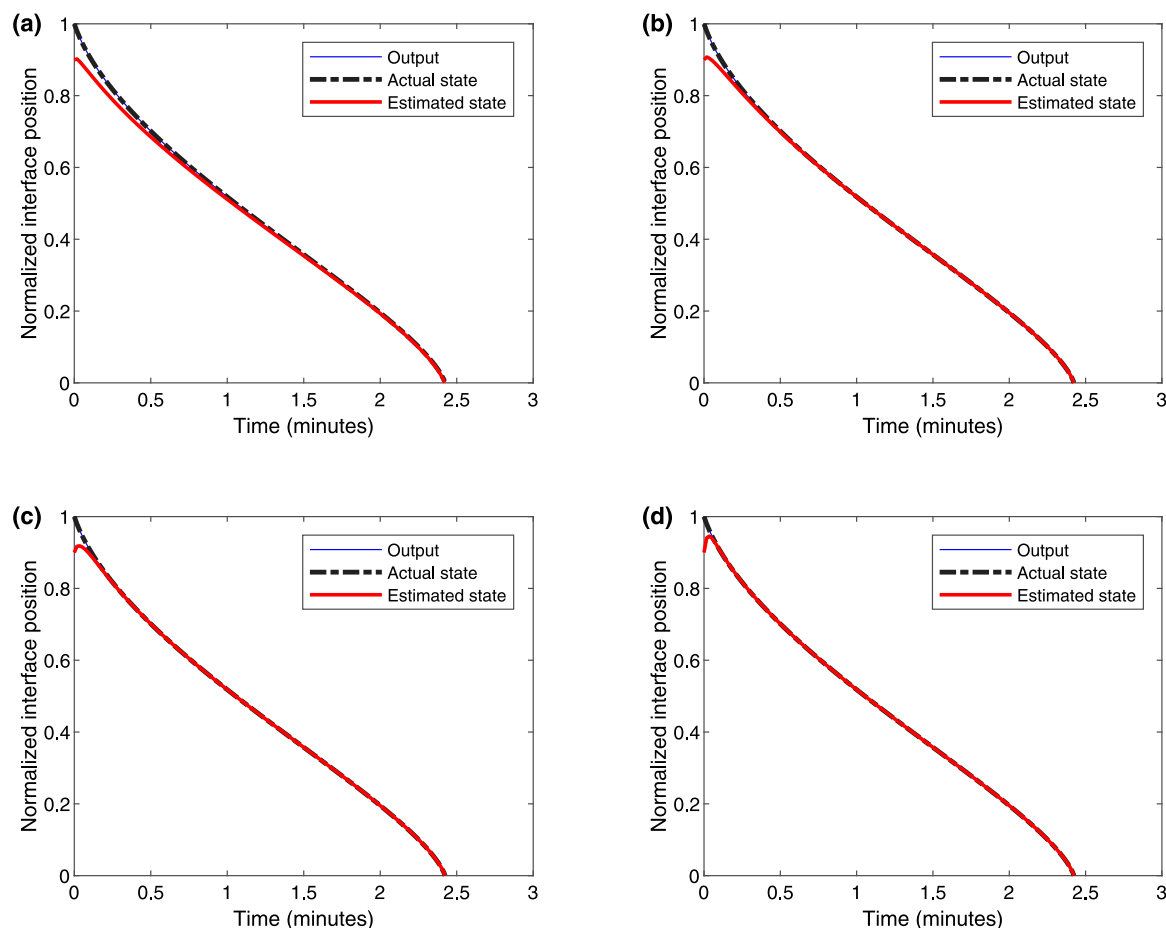


Fig. 9. Simulated time evolution of the actual, measured, and estimated position of the solid–liquid interface for values of the observer gain (a) $L_3 = -1/2$, (b) $L_3 = -2$, (c) $L_3 = -5$, and (d) $L_3 = -15$, noise-free case. The observer gains L_1 and L_2 are -1 . The vial radius is 5 mm, and the heater temperature is 37°C. The initial interface position of the observer (red curve) is different from the actual initial state (black curve) to assess convergence. The output (blue curve) and actual state (black curve) are identical as there is no measurement noise.

not a concern because it comes at the very end of the process after the mass fraction of the solid is 5%, where the thawing process should be terminated. The interface position estimates have low sensitivity to measurement noise for all four values of the observer gain, with $L_3 = -5$ having the fastest speed of convergence. As a result, all subsequent simulations use the observer gain $L_3 = -5$.

The actual sensor noise in the experiment (Fig. 11) is not as strong as the sensor noise assumed based on the equipment specification of the thermal imaging camera (Fig. 10). The observer gain could be made larger in magnitude to improve convergence, but the observer would have higher sensitivity to noise. Since the observer converges efficiently with $L_3 = -5$, it is reasonable to use this gain to provide some margin for the observer to work well even with larger sensor noise, e.g., if some electronic equipment comes within the vicinity of the thermal imaging system.

5.2.2. Comparison of output measurement sets

The above derivations and results assume that all state measurements including the temperature profiles and interface position are available, which is valid for our thermal imaging camera setup. A drawback of such an estimator is that the temperature readings from thermal imaging can be inaccurate for low temperatures. For example, while the thermal imaging camera used in this work, FLIR A35sc, can read the temperature down to -40°C with an accuracy of $\pm 5^\circ\text{C}$ (FLIR, 2018), the minimum temperature of our system is -80°C . Potential sensor bias motivates the design of an observer whose only measurement input is the interface position. In this case, the output matrices C_1 and C_2 in

(51)–(54) are zero, and L_1 and L_2 are no longer design parameters of the observer.

Dropping the temperature profile measurements from the observer only has a very small effect on the observer performance (Fig. 12). The estimated profiles are almost identical (Fig. 12a) with the difference in the estimated interface position of less than 0.01 (i.e., 1% of the vial radius) most of the time except for the end of the process where the error is slightly higher (Fig. 12b). These results indicate that the observer requires only the interface position measurement, which means only the observer gain L_3 is important in the observer design. Since the simplified observer does not receive any image data at low temperature values (much below the melting point), this observer is robust to such sensor bias.

5.3. Real-time state estimation

The numerical model integrated with the observer was employed to perform real-time state estimation of the cell thawing process, focusing on tracking the moving solid–liquid interface and controlling the final mass fraction of the solid.

Fig. 13 compares the interface position predicted by the first-principles model and observer initialized by the measured temperatures and interface position at time $t = 0$ with the measured interface position throughout the thawing. The measurement and prediction of the first-principles model are the same as those shown in Fig. 8, with the observer prediction added for comparison. As expected, the observer updating (50) corrects for the inevitable uncertainty in the

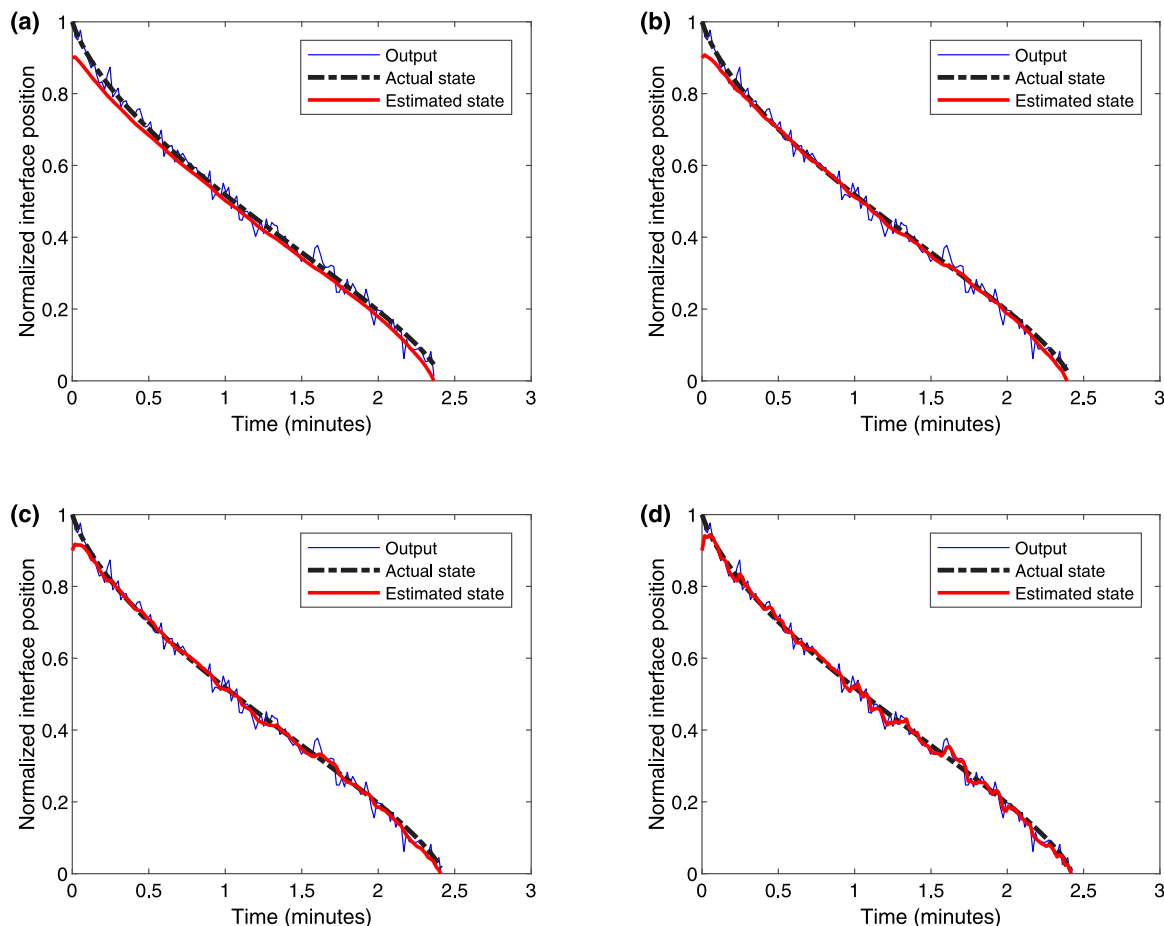


Fig. 10. Simulated time evolution of the actual, measured, and estimated position of the solid–liquid interface for values of the observer gain (a) $L_3 = -1/2$, (b) $L_3 = -2$, (c) $L_3 = -5$, and (d) $L_3 = -15$, with random measurement noise with the maximum of 5°C and minimum of -5°C given by the accuracy of the thermal imaging camera (FLIR, 2018). The observer gains L_1 and L_2 are -1 . The vial radius is 5 mm, and the heater temperature is 37°C . The initial interface position of the observer (red curve) is different from the actual initial state (black curve) to assess convergence.

first-principles model when determining the estimated interface position. The difference between the measured and estimated interface position is about 1%–2% except for the last few seconds where the error slightly increases. In addition, the observer filters the noise in the measurement of the interface position.

The observer was repeatedly tested under the given operating conditions (Fig. 14). In all cases, the observer accurately tracks the solid–liquid interface position through the end of the thawing process while filtering the measurement noise. The experimental performance over many runs provides confidence that the observer can be used to reliably control the cell thawing process.

The observer design is also capable of handling a thermal imaging camera that has larger sensor noise. While some noise can be observed in the measured interface position (Fig. 14), the noise is relatively modest. The sensor noise can be larger, for example, when the spatial resolution of the thermal imaging camera is lower, or there is interference from electronic devices or other light sources. Fig. 15 considers the same measurement data as in Fig. 14, except with independent normally distributed noise of standard deviation given by $3\sigma = 5^\circ\text{C}$ added to each pixel, which is based on the error range reported in the user manual for the thermal imaging camera (FLIR, 2018). Our observer can give good interface position estimates even with very noisy data. The observer has the most value for determining the endpoint of cell thawing when the thermal imaging data are noisy.

Besides noise filtering and interface position estimation, the approach taken in this article captures all the important physics of the system. As such, the approach can be readily extended to a wide range

of applications including optimal control and model predictive control, which is useful in some cell thawing scenarios where the heater temperature needs to be manipulated (Jang et al., 2017; Baboo et al., 2019). The observer also has better performance than alternative approaches that are more straightforward such as using a simple mechanistic model in the observer, or using a low-pass filter (see Appendix D).

It is important to note that the numerical model and observer presented and tested in this work are based on thawing in one dimension. Nevertheless, in reality, frozen material is also heated from the bottom. As a result, vertical thawing can influence the final mass fraction of the frozen material. This deviation and possible correction regarding heat transfer in the vertical direction are briefly discussed in Appendix E.

6. Conclusion

This work proposes a strategy for the dynamic simulation, state estimation, and control of the Stefan problems and applies the strategy to cell thawing. The first-principles model of cell thawing is derived from the one-dimensional two-phase Stefan problem defined in the cylindrical coordinate system. A finite difference approximation is combined with the method of lines in a moving grid domain, which is a more accurate numerical scheme than typical fixed grid approaches and facilitates observer and control design. State estimation and control of the Stefan problem can be achieved by building the Luenberger observer upon the first-principles model with inputs from real-time thermal imaging of cells. With an optimal observer gain design, the

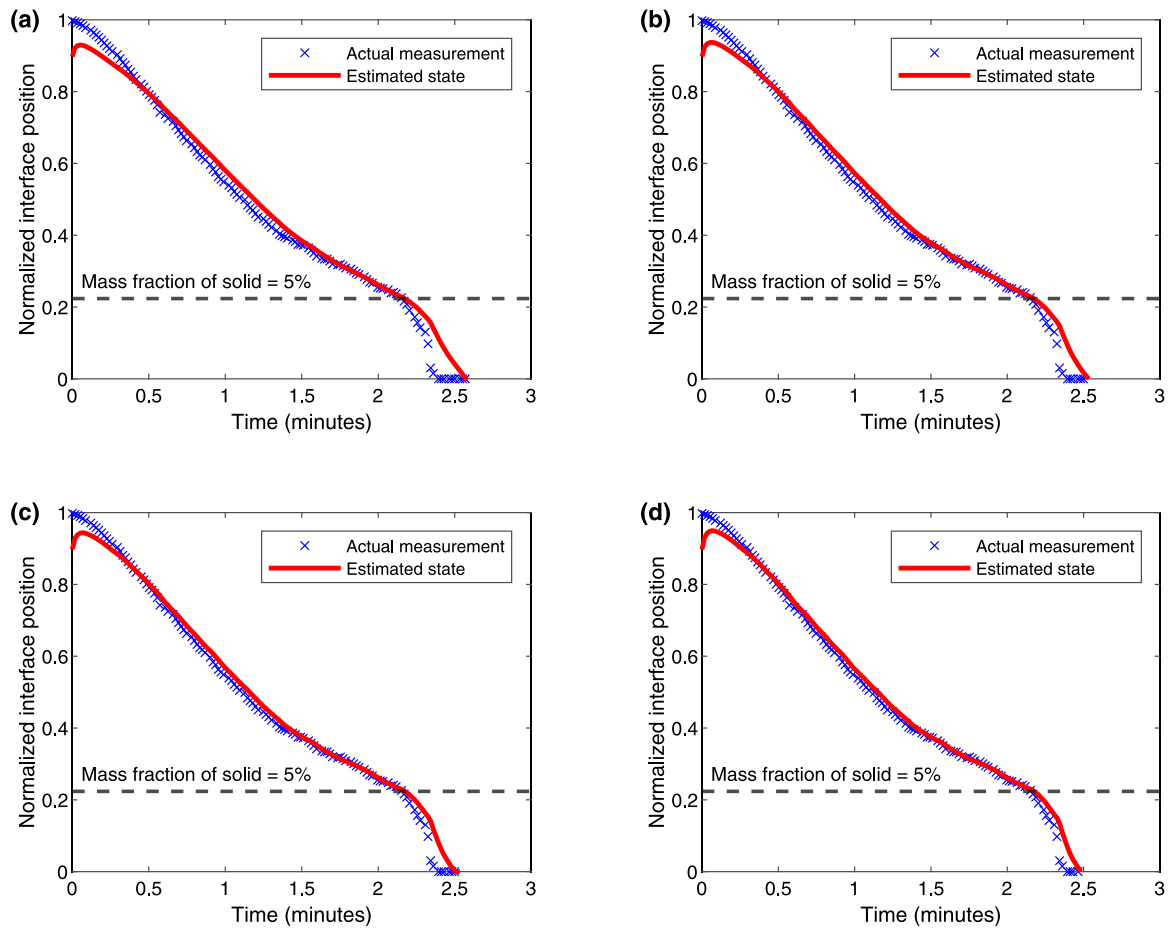


Fig. 11. Time evolution of the measured and estimated position of the solid-liquid interface for values of the observer gain (a) $L_3 = -2$, (b) $L_3 = -3$, (c) $L_3 = -4$, and (d) $L_3 = -5$. The observer gains L_1 and L_2 are -1 . The vial radius is 5 mm, and the heater temperature is 37°C. The initial interface position of the observer is different from the initial measured value to demonstrate convergence; in practice, this value can be set to the initial measured value.

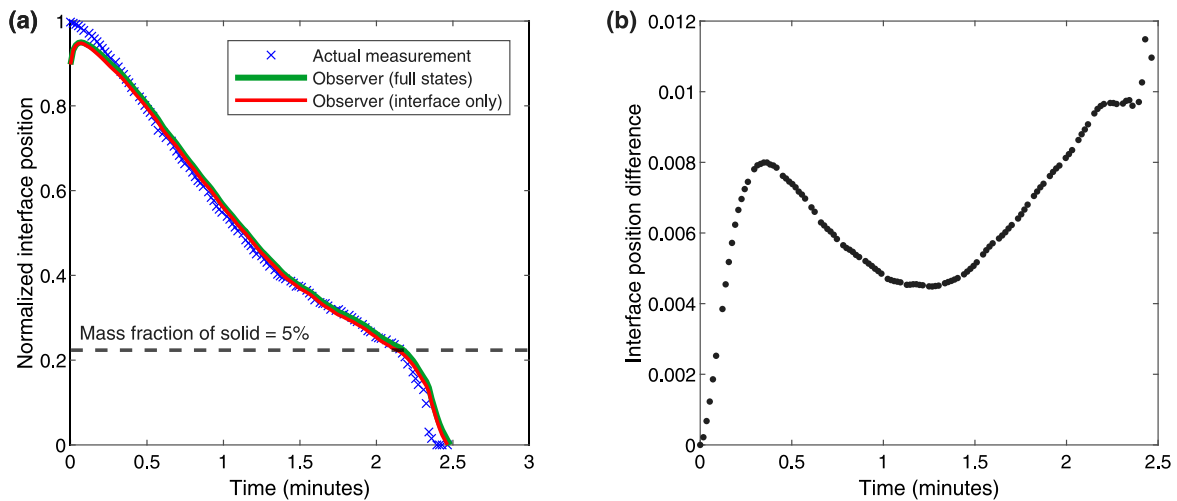


Fig. 12. Time evolution of the (a) estimated position of the solid-liquid interface when both temperature and interface position are measurable, and only the interface position can be measured and (b) pointwise difference between the results obtained from both approaches. The observer gain L_3 is -5 in all cases with $L_1 = L_2 = -1$ for the case with temperature measurements (full states). Other parameters and data are the same as those in Fig. 11.

observer corrects the states in the first-principles model while being insensitive to model uncertainty and measurement noise.

The numerical model and observer were employed in an experimental cell thawing process for real-time state estimation and control of the moving solid-liquid interface. The first-principles model simulates

the evolution of the solid-liquid interface with errors of less than 5% when the solid phase dominates, and more than 10% when the system contains mostly liquid. The integrated model and observer can accurately predict the interface position within about 1%–2% throughout the process in all experimental runs.

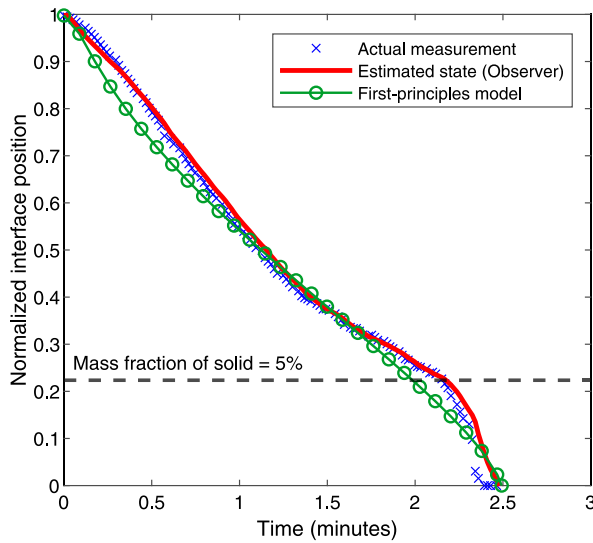


Fig. 13. Time evolution of the measured, estimated, and predicted interface position for the vial radius of 5 mm and heater temperature of 37°C. The observer gains are $L_1 = L_2 = -1$ and $L_3 = -5$, taking a complete set of measurements (temperature and interface position). The first-principles model and observer are initialized by the measured initial temperatures and interface position.

Some potential future directions would be to develop a model and design an observer for a system with more spatial dimensions, take into account temperature-dependent properties, include convective heat transfer into the model, and explore advanced control systems design.

CRedit authorship contribution statement

Prakrit Srisuma: Formal analysis, Funding acquisition, Investigation, Methodology, Software, Validation, Visualization, Writing – original draft, Writing – review & editing. **Ajinkya Pandit:** Investigation, Methodology, Software, Supervision, Validation, Visualization, Writing – original draft, Writing – review & editing. **Qihang Zhang:** Formal analysis, Investigation, Methodology, Software, Validation, Visualization, Writing – review & editing. **Moo Sun Hong:** Investigation, Methodology, Software, Validation, Writing – review & editing. **Janaka Gamekkanda:** Investigation, Methodology, Validation, Writing – review & editing. **Fabio Fachin:** Conceptualization, Funding acquisition, Writing – review & editing. **Nathan Moore:** Conceptualization, Writing – review & editing. **Dragan Djordjevic:** Conceptualization, Writing – review & editing. **Michael Schwaerzler:** Conceptualization, Funding acquisition, Project administration, Writing – review & editing. **Tolutola Oyetunde:** Conceptualization, Funding acquisition, Project administration, Writing – review & editing. **Wenlong Tang:** Project administration, Writing – review & editing. **Allan S. Myerson:** Conceptualization, Funding acquisition, Methodology, Project administration, Resources, Supervision, Validation, Writing – review & editing. **George Barbastathis:** Conceptualization, Funding acquisition, Methodology, Project administration, Resources, Supervision, Validation, Writing – review & editing. **Richard D. Braatz:** Formal analysis, Conceptualization, Funding acquisition, Methodology, Project administration, Resources, Supervision, Validation, Visualization, Writing – original draft, Writing – review & editing.

Declaration of competing interest

The authors declare that they have no known competing financial interests or personal relationships that could have appeared to influence the work reported in this paper.

Data availability

Data will be made available on request.

Acknowledgments

This research was supported, in part, by Takeda Development Center Americas, Inc. (successor in interest to Millennium Pharmaceuticals, Inc.), United States of America and a Fulbright Program grant sponsored by the Bureau of Educational and Cultural Affairs of the United States Department of State and administered by the Institute of International Education.

Appendix A. Fixed grid dimensionalization

A common nondimensionalization technique for heat transfer problems in the radial direction is to define the normalized radius

$$R = \frac{r}{b}, \quad (\text{A.1})$$

where other variables and constants are the same as those defined in Section 2.4. As a result, the governing equations for the solid region ($0 < R < S$) and liquid region ($S < R < 1$) can be written as

$$\frac{\partial \Theta_1}{\partial \tau} = \frac{\partial^2 \Theta_1}{\partial R^2} + \frac{1}{R} \frac{\partial \Theta_1}{\partial R}, \quad (\text{A.2})$$

$$\frac{1}{\alpha_0} \frac{\partial \Theta_2}{\partial \tau} = \frac{\partial^2 \Theta_2}{\partial R^2} + \frac{1}{R} \frac{\partial \Theta_2}{\partial R}. \quad (\text{A.3})$$

The Robin boundary condition at $R = 1$ is

$$\begin{cases} \frac{\partial \Theta_1}{\partial R} = U_0 k_0 (1 - \Theta_1) & \text{for } \tau \leq \tau_s, \\ \frac{\partial \Theta_2}{\partial R} = U_0 (1 - \Theta_2) & \text{for } \tau > \tau_s. \end{cases} \quad (\text{A.4})$$

For the symmetry condition at $R = 0$,

$$\begin{cases} \frac{\partial \Theta_1}{\partial R} = 0 & \text{for } \tau < \tau_l, \\ \frac{\partial \Theta_2}{\partial R} = 0 & \text{for } \tau \geq \tau_l. \end{cases} \quad (\text{A.5})$$

Finally, the Stefan conditions at $R = S$ for $\tau_s < \tau < \tau_l$ include the melting point condition having the same form as (29), and the energy balance that becomes

$$\frac{1}{\text{Ste}} \frac{dS}{d\tau} = \frac{\partial \Theta_1}{\partial R} - k_0 \frac{\partial \Theta_2}{\partial R}. \quad (\text{A.6})$$

Discretization of the above equations results in a fixed grid domain, i.e., the space between each grid point is constant and does not change with time. This approach is straightforward to implement numerically but requires adding or subtracting grid points in the two domains when the solid–liquid interface moves, and tracking the time-varying distance between grid points near the interface (see Appendix B).

Appendix B. Numerical methods for fixed grids

Applying the central difference (second-order accurate) approximation to the spatially dependent terms and the forward Euler method to the time-dependent terms in (A.2) and (A.3) transforms the PDEs into the difference equations

$$\frac{(\Theta_1)_{i+1}^{k+1} - (\Theta_1)_i^k}{\Delta \tau} = \frac{(\Theta_1)_{i+1}^k - 2(\Theta_1)_i^k + (\Theta_1)_{i-1}^k}{(\Delta R)^2} + \frac{(\Theta_1)_{i+1}^k - (\Theta_1)_{i-1}^k}{2i(\Delta R)^2}, \quad (\text{B.1})$$

$$\frac{(\Theta_2)_{i+1}^{k+1} - (\Theta_2)_i^k}{\alpha_0 \Delta \tau} = \frac{(\Theta_2)_{i+1}^k - 2(\Theta_2)_i^k + (\Theta_2)_{i-1}^k}{(\Delta R)^2} + \frac{(\Theta_2)_{i+1}^k - (\Theta_2)_{i-1}^k}{2i(\Delta R)^2}, \quad (\text{B.2})$$

where $\Delta R = 1/n$ is the distance between adjacent grid points in the radial direction, i is the integer index in the radial direction ($R = i\Delta R$), $\Delta \tau$ is the time step, and k is the integer index along the time axis

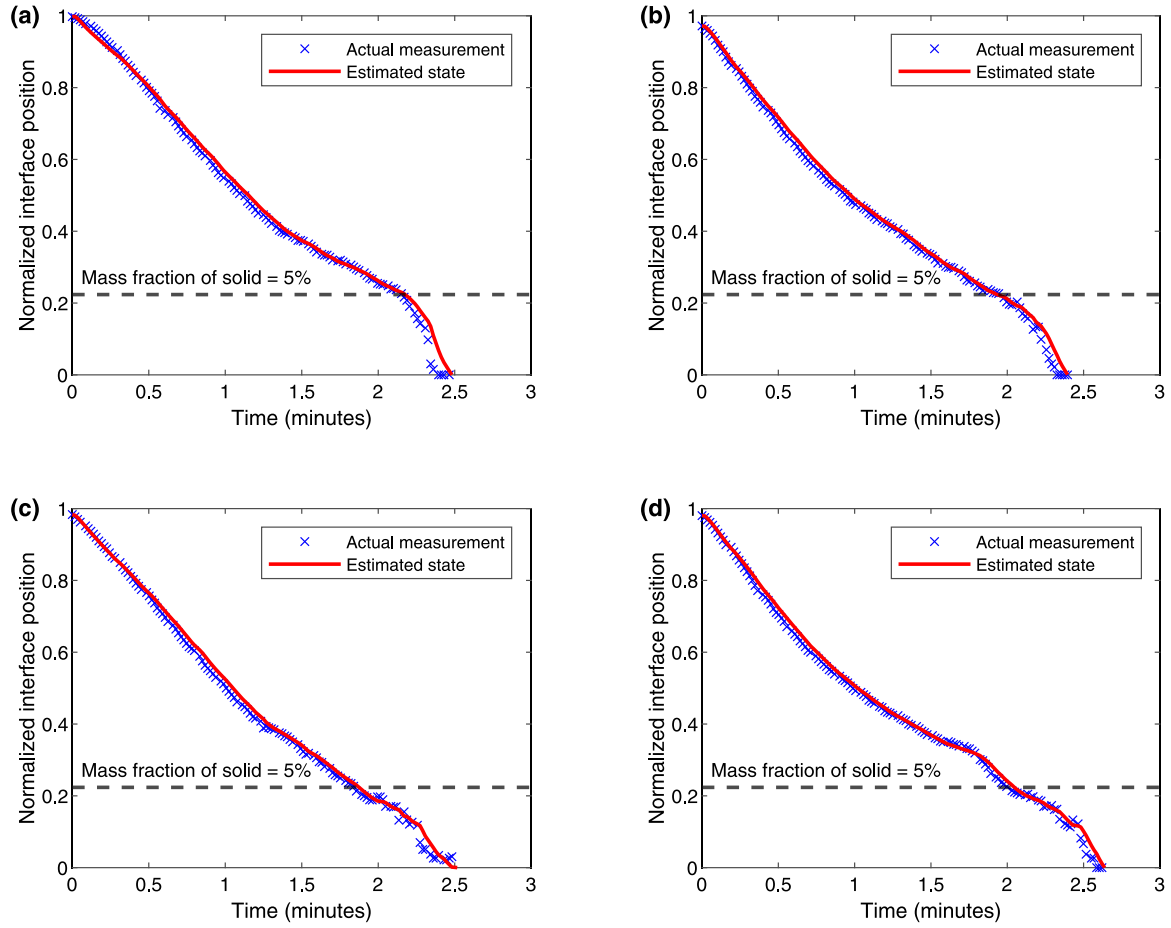


Fig. 14. Time evolution of the estimated and measured interface position from four experimental runs for the vial radius of 5 mm and heater temperature of 37°C. The observer gains are $L_1 = L_2 = -1$ and $L_3 = -5$, taking a complete set of measurements (temperature and interface position). The observer is initialized by the measured initial temperatures and interface position.

($\tau = k\Delta\tau$). The above difference equations can be solved iteratively by rearranging to give

$$(\Theta_1)_i^{k+1} = (\Theta_1)_i^k + \frac{\Delta\tau}{(\Delta R)^2} \left(\left(1 + \frac{1}{2i}\right) (\Theta_1)_{i+1}^k - 2(\Theta_1)_i^k + \left(1 - \frac{1}{2i}\right) (\Theta_1)_{i-1}^k \right), \quad (\text{B.3})$$

$$(\Theta_2)_i^{k+1} = (\Theta_2)_i^k + \frac{\alpha_0 \Delta\tau}{(\Delta R)^2} \left(\left(1 + \frac{1}{2i}\right) (\Theta_2)_{i+1}^k - 2(\Theta_2)_i^k + \left(1 - \frac{1}{2i}\right) (\Theta_2)_{i-1}^k \right). \quad (\text{B.4})$$

Applying the central difference scheme to the Robin boundary condition results in

$$\begin{cases} \frac{(\Theta_1)_{n+1}^k - (\Theta_1)_{n-1}^k}{2\Delta R} = U_0 k_0 (1 - (\Theta_1)_n^k) & \text{for } \tau \leq \tau_s, \\ \frac{(\Theta_2)_{n+1}^k - (\Theta_2)_{n-1}^k}{2\Delta R} = U_0 (1 - (\Theta_2)_n^k) & \text{for } \tau > \tau_s. \end{cases} \quad (\text{B.5})$$

The symmetry condition at the center reformulated by L'Hôpital's rule is

$$\begin{cases} \frac{(\Theta_1)_0^{k+1} - (\Theta_1)_0^k}{\Delta\tau} = \frac{4}{(\Delta R)^2} ((\Theta_1)_1^k - (\Theta_1)_0^k) & \text{for } \tau < \tau_l, \\ \frac{(\Theta_2)_0^{k+1} - (\Theta_2)_0^k}{\Delta\tau} = \frac{4\alpha_0}{(\Delta R)^2} ((\Theta_2)_1^k - (\Theta_2)_0^k) & \text{for } \tau \geq \tau_l. \end{cases} \quad (\text{B.6})$$

The Stefan conditions are

$$(\Theta_1)_p^k = (\Theta_2)_p^k = 0, \quad (\text{B.7})$$

$$\frac{1}{\text{Ste}} \left(\frac{S^{k+1} - S^k}{\Delta\tau} \right) = \left(\frac{3(\Theta_1)_p^k}{2\Delta R} - \frac{2(\Theta_1)_{p-1}^k}{\Delta R} + \frac{(\Theta_1)_{p-2}^k}{2\Delta R} \right) - k_0 \left(-\frac{3(\Theta_2)_p^k}{2\Delta R} + \frac{2(\Theta_2)_{p+1}^k}{\Delta R} - \frac{(\Theta_2)_{p+2}^k}{2\Delta R} \right), \quad (\text{B.8})$$

where $S = p\Delta R$ varies between 0 and 1, and p is the position index of the moving interface (Fig. B.1) rounded to the closest integer.

A drawback of solving the difference equations iteratively is that the time step $\Delta\tau$ is required to be small to ensure numerical stability, which is not computationally efficient. To avoid this issue, the PDEs can be alternatively handled by using the numerical method of lines (employed in the main paper), which discretizes the spatial derivatives only, converting each PDE into a system of ODEs. In this case, the discretized governing equations are

$$\frac{d(\Theta_1)_i}{d\tau} = \frac{(\Theta_1)_{i+1} - 2(\Theta_1)_i + (\Theta_1)_{i-1}}{(\Delta R)^2} + \frac{(\Theta_1)_{i+1} - (\Theta_1)_{i-1}}{2i(\Delta R)^2}, \quad (\text{B.9})$$

$$\frac{1}{\alpha_0} \frac{d(\Theta_2)_i}{d\tau} = \frac{(\Theta_2)_{i+1} - 2(\Theta_2)_i + (\Theta_2)_{i-1}}{(\Delta R)^2} + \frac{(\Theta_2)_{i+1} - (\Theta_2)_{i-1}}{2i(\Delta R)^2}. \quad (\text{B.10})$$

The Robin boundary condition is

$$\begin{cases} \frac{(\Theta_1)_{n+1} - (\Theta_1)_{n-1}}{2\Delta R} = U_0 k_0 (1 - (\Theta_1)_n) & \text{for } \tau \leq \tau_s, \\ \frac{(\Theta_2)_{n+1} - (\Theta_2)_{n-1}}{2\Delta R} = U_0 (1 - (\Theta_2)_n) & \text{for } \tau > \tau_s. \end{cases} \quad (\text{B.11})$$

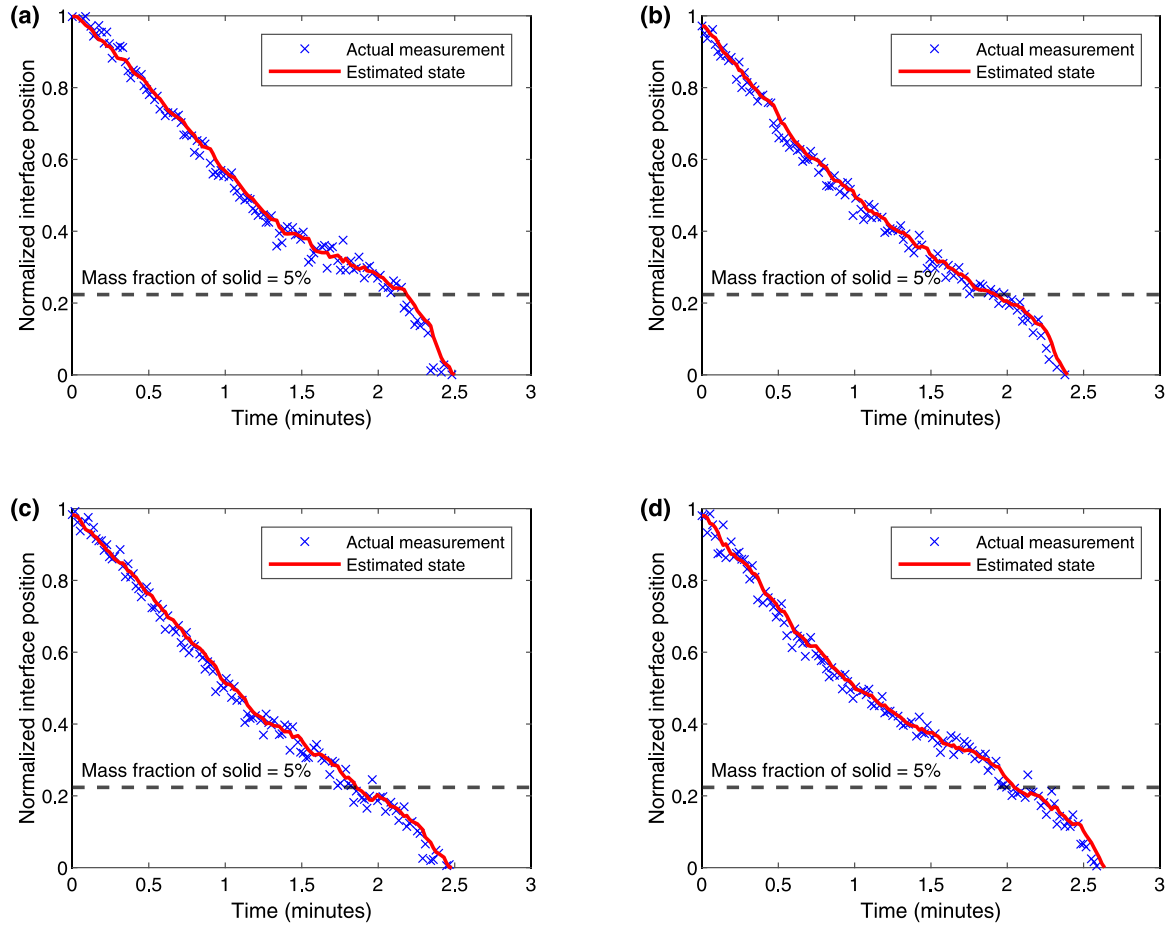


Fig. 15. Time evolution of the estimated and measured interface position from four experimental runs for the vial radius of 5 mm and heater temperature of 37°C. The observer gains are $L_1 = L_2 = -1$ and $L_3 = -5$, taking the same set of measurements as in Fig. 14 but with stronger sensor noise. The observer is initialized by the measured initial temperatures and interface position.

The symmetry condition becomes

$$\begin{cases} \frac{d(\Theta_1)_0}{d\tau} = \frac{4}{(\Delta R)^2} ((\Theta_1)_1 - (\Theta_1)_0) & \text{for } \tau < \tau_l, \\ \frac{d(\Theta_2)_0}{d\tau} = \frac{4\alpha_0}{(\Delta R)^2} ((\Theta_2)_1 - (\Theta_2)_0) & \text{for } \tau \geq \tau_l. \end{cases} \quad (\text{B.12})$$

The Stefan conditions are

$$(\Theta_1)_p = (\Theta_2)_p = 0, \quad (\text{B.13})$$

$$\frac{1}{\text{Ste}} \frac{dS}{d\tau} = \left(\frac{3(\Theta_1)_p}{2\Delta R} - \frac{2(\Theta_1)_{p-1}}{\Delta R} + \frac{(\Theta_1)_{p-2}}{2\Delta R} \right) - k_0 \left(-\frac{3(\Theta_2)_p}{2\Delta R} + \frac{2(\Theta_2)_{p+1}}{\Delta R} - \frac{(\Theta_2)_{p+2}}{2\Delta R} \right). \quad (\text{B.14})$$

In comparison with the technique presented Section 3, this approach is easier to implement as the discretization is straightforward, and the PDEs/ODEs are linear. Nevertheless, there are significant disadvantages. Figs. B.1 and B.2 pictorially illustrate the discretization of the fixed grid domain and evolution of the moving interface, respectively. The indices are $i = 0$ at the center to $i = n$ at the outer boundary. The interface position is labeled with the index p . With this approach, the space between each grid is always constant, i.e., does not change with time. In addition, the total number of grid points is fixed at $n + 1$. The number of grid points in each phase, however, varies as the moving interface moves, i.e., as the index p changes. As such, the number of grids in each region changes with time. In terms of numerical solutions, this change can cause some issues at the beginning of thawing because the number of grid points in the liquid phase is low during this time. For

example, when $p = n - 1$, there is only one grid point in the liquid region, and having only one grid point to capture a high temperature gradient in the liquid phase results in an inaccurate solution. The same issue can occur when thawing almost completes, i.e., the solid region is small. Another problem of this approach is that variation in the number of grid points implies that the number of states in each region is not constant, which is not preferable in state estimation and process control. These issues can be avoided by using the moving grid technique proposed in Sections 2.4 and 3.

Appendix C. Thermal imaging data analysis

The spatial temperature fields recorded by the thermal imaging camera indicate radial symmetry during thawing (Fig. C.1). The temperature map was interpolated linearly between pixels to obtain the temperature corresponding to each grid point for the numerical model.

The radial position of the solid-liquid interface from the measurement (y_3) can be determined by

$$y_3 = \sqrt{\frac{A_s}{A_t}}, \quad (\text{C.1})$$

where A_s is the circle area covering the solid phase, i.e., the region with temperatures lower than the melting point of -2°C , and A_t is the total circle area of the cell vial. By connecting the camera to MATLAB, the temperature profile and interface position were extracted from each spatial temperature field and recorded every second.

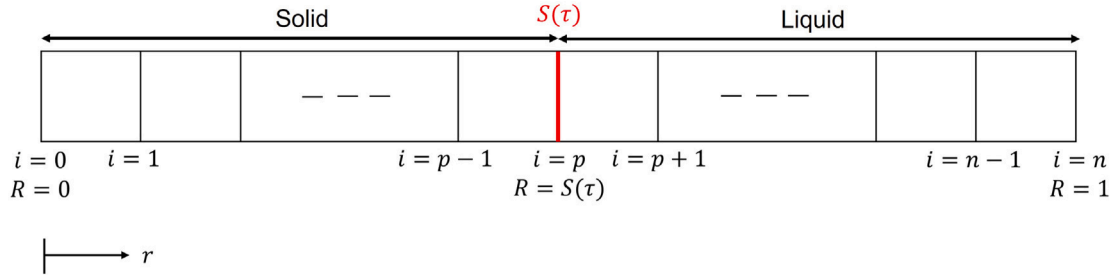


Fig. B.1. Discretization of the fixed grid domain.

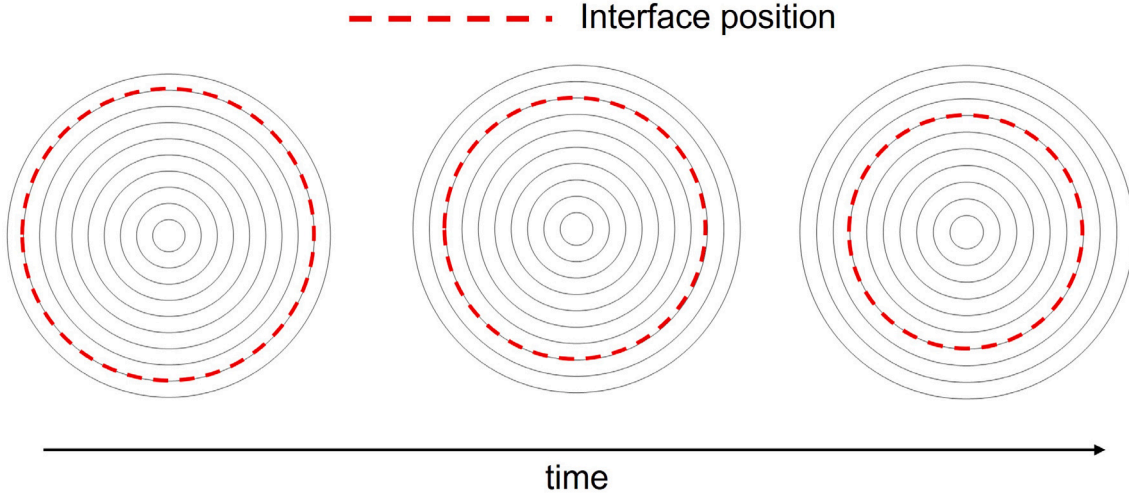


Fig. B.2. Evolution of the solid-liquid interface in the fixed grid domain.

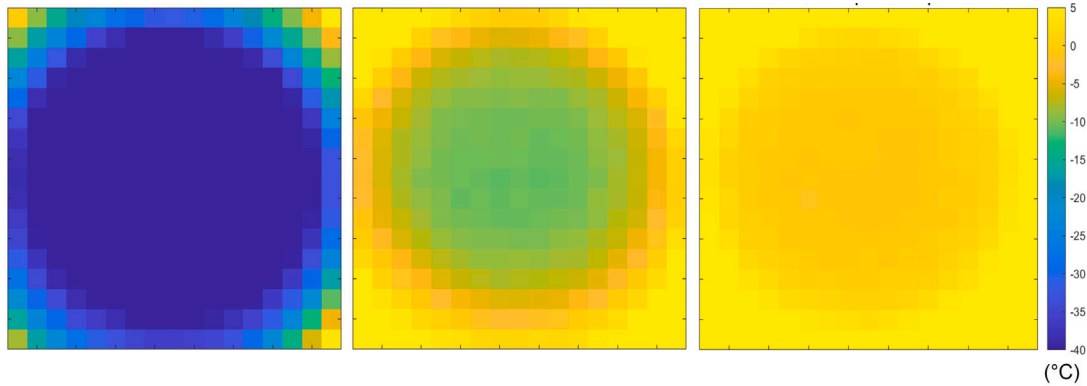


Fig. C.1. Spatial temperature fields recorded by the thermal imaging camera.

Appendix D. Simple model and low-pass filter

As discussed in Section 5.3, the proposed observer is able to estimate the interface position despite noisy measurement. The observer relies on numerical simulation of the mechanistic model derived from the Stefan problem integrated with the Luenberger observer; we denote this approach as the Luenberger observer in this appendix. Two simpler alternatives for interface position estimation are using (1) a simple model in the observer or (2) a low-pass filter.

For the simple model, the speed of the interface position can be assumed constant at v , which is corrected by an observer. Modifying (50) results in

$$\frac{d\hat{x}_3}{d\tau} = -v + L_v(\hat{y}_3 - y_3), \quad (\text{D.1})$$

where L_v is the observer gain for this simple model, which is the only design parameter. This approach does not model the heat transfer in the system, and so is simpler than our framework.

For the low-pass filter, the measurement is filtered using an exponential filter,

$$\tau_F \frac{d\hat{y}_3}{d\tau} + \hat{y}_3 = y_3, \quad (\text{D.2})$$

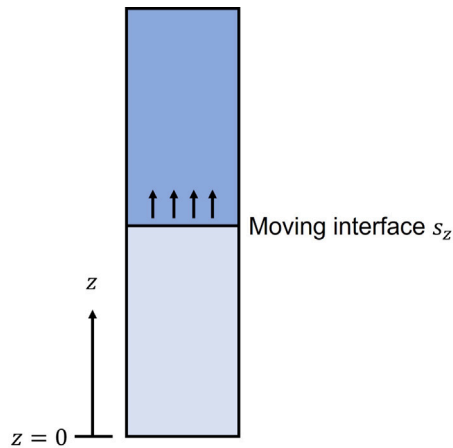
where τ_F is the only design parameter.

To compare the three approaches, consider the base case where all the parameters are as given in Table 1. The correct interface position (actual state) is obtained by simulating the first-principles model (45)–(47). The noisy measurement is created by adding random measurement noise of $\pm 5^\circ\text{C}$ to the actual state. The Luenberger observer, simple model, and low-pass filter are applied to that noisy measurement

Table D.1

Comparison between the interface position errors of the Luenberger observer, simple model, and low-pass filter. The optimal values of L_v and τ_F are used for the simple model observer and low-pass filter.

Approach	Interface position error	
	RMS	Maximum
Luenberger observer	0.0070	0.0254
Simple model	0.0116	0.0264
Low-pass filter	0.0170	0.0380

**Fig. E.1.** Vertical moving interface.

for interface position estimation, with estimation errors reported in Table D.1. Quantitatively, the Luenberger observer gives a significantly more accurate estimation of the interface position – both in terms of the root-mean-square (RMS) and maximum errors – than the simple model and low-pass filter.

In addition to having the highest accuracy, our framework captures all the important physics of the system and therefore can be employed for additional applications such as optimal control and model predictive control of cell thawing. Although the simple model and low-pass filter are computationally much cheaper than the Luenberger observer, all of the approaches are implementable in real time for this application. While the number of floating point calculations in the Luenberger observer is orders of magnitude higher than for the simple estimation methods, the Luenberger observer still only requires simulation, which is orders of magnitude less expensive than more advanced observers, e.g., moving horizon estimation and particle filtering.

Appendix E. Vertical thawing correction

Although the observer design presented in this work is based on thawing in one dimension (r), thawing in the vertical direction (z) at the bottom of the frozen material would affect the mass fraction of the solid (Fig. E.1). This section estimates the error caused by neglecting vertical thawing.

If the bottom of the vial has curvature similar to its sides, then the thickness of liquid at the bottom of the vial will be nearly the same as the thickness of liquid on the sides (Deen, 1998), and this can be used to correct the fraction of frozen material. For example, for frozen material of height of 43 mm in a vial of radius 5 mm, the height of 43 mm would be corrected to $43 - 4 = 39$ mm when the frozen material has a radius of 1 mm. This correction to the mass of frozen material would be $(43 - 39)/43 = 9.3\%$.

For a vial bottom that is flat, a somewhat more involved analysis results in a similar estimate for the thickness of liquid at the bottom of the vial. As explained and derived in Carslaw and Jaeger (1959), the motion of the solid–liquid interface in the vertical direction can be

approximated using a similarity solution.² The interface position in the vertical direction (s_z) is given by

$$s_z = \lambda \sqrt{4\alpha_2 t}, \quad (\text{E.1})$$

where λ is a constant that satisfies the relation

$$\lambda e^{\lambda^2} \operatorname{erf} \lambda = \frac{C_{p2}(T_0 - T_m)}{\Delta H_f \sqrt{\pi}}. \quad (\text{E.2})$$

From the results shown in Section 5.3, the time scale of thawing is around 2.5 min. With this time scale, the vertical interface position s_z is about 4 mm, which should be considered in comparison to the height of our vial of about 43 mm. Hence, the error when neglecting vertical thawing is about 10% in the solid mass fraction. This error is not negligible but also not significant enough to prevent the one-dimensional model from working reliably. This small correction can be simply added to the current model to obtain a more accurate prediction of the solid fraction of frozen material.

References

- Abdulla, U.G., Poggi, B., 2019. Optimal control of the multiphase Stefan problem. *Appl. Math. Optim.* 80, 479–513, URL: <https://doi.org/10.1007/s00245-017-9472-7>.
- Baboo, J., Kilbride, P., Delahaye, M., Milne, S., Fonseca, F., Blanco, M., Meneghel, J., Nancekivell, A., Gaddum, N., Morris, G.J., 2019. The impact of varying cooling and thawing rates on the quality of cryopreserved human peripheral blood T cells. *Sci. Rep.* 9, 3417, URL: <https://doi.org/10.1038/s41598-019-39957-x>.
- Bird, R.B., Lightfoot, E.N., Stewart, W.E., 2002. *Transport Phenomena*, second ed. John Wiley & Sons, New York.
- Bollati, J., Tarzia, D.A., 2018. One-phase Stefan-like problems with latent heat depending on the position and velocity of the free boundary and with Neumann or Robin boundary conditions at the fixed face. *Math. Probl. Eng.* 2018, 4960391, URL: <https://doi.org/10.1155/2018/4960391>.
- Brezina, M., Klimes, L., Stetina, J., 2018. Optimization of material properties of phase change materials for latent heat thermal energy storage. *MENDEL* 24 (1), 47–54, URL: <https://doi.org/10.13164/mendel.2018.1.047>.
- Brosa Planella, F., Please, C.P., Van Gorder, R.A., 2019. Extended Stefan problem for solidification of binary alloys in a finite planar domain. *SIAM J. Appl. Math.* 79 (3), 876–913, URL: <https://doi.org/10.1137/18M118699X>.
- Brosa Planella, F., Please, C.P., Van Gorder, R.A., 2021. Extended Stefan problem for the solidification of binary alloys in a sphere. *European J. Appl. Math.* 32 (2), 242–279, URL: <https://doi.org/10.1017/S095679252000011X>.
- Carslaw, H., Jaeger, J., 1959. *Conduction of Heat in Solids*, second ed. Oxford University Press, London.
- Cottle, C., Porter, A.P., Lipat, A., Turner-Lyles, C., Nguyen, J., Moll, G., Chinnadurai, R., 2022. Impact of cryopreservation and freeze-thawing on therapeutic properties of mesenchymal stromal/stem cells and other common cellular therapeutics. *Curr. Stem Cell Rep.* 8 (2), 72–92, URL: <https://doi.org/10.1007/s40778-022-00212-1>.
- Crank, J., 1975. *The Mathematics of Diffusion*, second ed. Oxford University Press, London.
- Dalwadi, M.P., Waters, S.L., Byrne, H.M., Hewitt, I.J., 2020. A mathematical framework for developing freezing protocols in the cryopreservation of cells. *SIAM J. Appl. Math.* 80 (2), 657–689, URL: <https://doi.org/10.1137/19M1275875>.
- Deen, W., 1998. *Analysis of Transport Phenomena*. Oxford University Press, New York.
- FLIR, 2018. *User's Manual FLIR Ax5 Series*. FLIR Systems, Portland.
- Ford Versypt, A.N., Braatz, R.D., 2014. Analysis of finite difference discretization schemes for diffusion in spheres with variable diffusivity. *Comput. Chem. Eng.* 71, 241–252, URL: <https://doi.org/10.1016/j.compchemeng.2014.05.022>.
- Friedman, A., Kinderlehrer, D., 1975. A one phase Stefan problem. *Indiana Univ. Math. J.* 24 (11), 1005–1035, URL: <http://www.jstor.org/stable/24890912>.
- Gusev, A.O., Shcheritsa, O.V., Mazhorova, O.S., 2021. Two equivalent finite volume schemes for Stefan problem on boundary-fitted grids: Front-tracking and front-fixing techniques. *Differential Equations* 57 (7), 876–890, URL: <https://doi.org/10.1134/S0012266121070053>.
- Hayashi, Y., Kino-oka, M., Sugiyama, H., 2022. Hybrid-model-based design of fill-freeze-thaw processes for human induced pluripotent stem cells considering productivity and quality. *Comput. Chem. Eng.* 156, 107566, URL: <https://doi.org/10.1016/j.compchemeng.2021.107566>.
- Hunt, C.J., 2019. Technical considerations in the freezing, low-temperature storage and thawing of stem cells for cellular therapies. *Transfus. Med. Hemotherapy* 46 (3), 134–149, URL: <https://doi.org/10.1159/000497289>.

² The similarity solution assumes that there is no heat transfer resistance between the vial and the material inside the vial, and the temperature gradient in the solid is negligible. As such, the analysis is slightly conservative.

- Jang, H., Lee, J.H., Braatz, R.D., Kim, K.-K.K., 2014. Fast moving horizon estimation for a two-dimensional distributed parameter system. *Comput. Chem. Eng.* 63, 159–172, URL: <https://doi.org/10.1016/j.compchemeng.2013.12.005>.
- Jang, T.H., Park, S.C., Yang, J.H., Kim, J.Y., Seok, J.H., Park, U.S., Choi, C.W., Lee, S.R., Han, J., 2017. Cryopreservation and its clinical applications. *Integr. Med. Res.* 6 (1), 12–18, URL: <https://doi.org/10.1016/j.imr.2016.12.001>.
- Kalman, R.E., 1960. A new approach to linear filtering and prediction problems. *J. Basic Eng.* 82 (1), 35–45.
- Kar, A., Mazumder, J., 1994. Analytical solution of the Stefan problem in finite mediums. *Quart. Appl. Math.* 52 (1), 49–58, URL: <https://www.jstor.org/stable/43637971>.
- Karabeni, H., Esen, A., Aksan, E., 2016. Numerical solutions for a Stefan problem. *New Trends Math. Sci.* 4 (4), 175–187, URL: <https://doi.org/10.20852/ntmsci.2016422668>.
- Khalid, M.Z., Zubair, M., Ali, M., 2019. An analytical method for the solution of two phase Stefan problem in cylindrical geometry. *Appl. Math. Comput.* 342, 295–308, URL: <https://doi.org/10.1016/j.amc.2017.09.013>.
- Koga, S., Diagne, M., Krstic, M., 2019. Control and state estimation of the one-phase Stefan problem via backstepping design. *IEEE Trans. Automat. Control* 64 (2), 510–525, URL: <https://doi.org/10.1109/TAC.2018.2836018>.
- Kumar, E.V., Jerome, J., Ayyappan, S., 2013. Comparison of four state observer design algorithms for MIMO system. *Arch. Control Sci.* 23, 243–256, URL: <https://doi.org/10.2478/acsc-2013-0015>.
- Kurbatova, G.I., Ermolaeva, N.N., 2019. An effective algorithm of the numerical solution to the Stefan problem. *J. Phys. Conf. Ser.* 1392, 012034, URL: <https://doi.org/10.1088/1742-6596/1392/1/012034>.
- Kutluay, S., Bahadir, A.R., Özdeş, A., 1997. The numerical solution of one-phase classical Stefan problem. *J. Comput. Appl. Math.* 81 (1), 135–144, URL: [https://doi.org/10.1016/S0377-0427\(97\)00034-4](https://doi.org/10.1016/S0377-0427(97)00034-4).
- Luenberger, D., 1971. An introduction to observers. *IEEE Trans. Automat. Control* 16 (6), 596–602, URL: .
- McCord, D., Crepeau, J., Siahpush, A., Ferres Brogin, J.A., 2016. Analytical solutions to the Stefan problem with internal heat generation. *Appl. Therm. Eng.* 103, 443–451, URL: <https://doi.org/10.1016/j.applthermaleng.2016.03.122>.
- Mesbah, A., Ford Versypt, A.N., Zhu, X., Braatz, R.D., 2014. Nonlinear model-based control of thin-film drying for continuous pharmaceutical manufacturing. *Ind. Eng. Chem. Res.* 53, 7447–7460, URL: <https://doi.org/10.1021/ie402837c>.
- Meyer, G.H., 1971. A numerical method for two-phase Stefan problems. *SIAM J. Numer. Anal.* 8 (3), 555–568, URL: <http://www.jstor.org/stable/2949674>.
- Mikova, V.V., Kurbatova, G.I., Ermolaeva, N.N., 2017. Analytical and numerical solutions to Stefan problem in model of the glaciation dynamics of the multilayer cylinder in sea water. *J. Phys. Conf. Ser.* 929, 012103, URL: <https://doi.org/10.1088/1742-6596/929/1/012103>.
- Mitchell, S., Vynnycky, M., 2014. On the numerical solution of two-phase Stefan problems with heat-flux boundary conditions. *J. Comput. Appl. Math.* 264, 49–64, URL: <https://doi.org/10.1016/j.cam.2014.01.003>.
- Mohd Ali, J., Ha Hoang, N., Hussain, M.A., Dochain, D., 2015. Review and classification of recent observers applied in chemical process systems. *Comput. Chem. Eng.* 76, 27–41, URL: <https://doi.org/10.1016/j.compchemeng.2015.01.019>.
- Petrus, B., Bentsman, J., Thomas, B.G., 2010. Feedback control of the two-phase Stefan problem, with an application to the continuous casting of steel. In: 49th IEEE Conference on Decision and Control. pp. 1731–1736, URL: <https://doi.org/10.1109/CDC.2010.5717456>.
- Popov, N., Tabakova, S., Feuillebois, F., 2005. Numerical modelling of the one-phase Stefan problem by finite volume method. In: Li, Z., Vulkov, L., Waśniewski, J. (Eds.), *Numerical Analysis and Its Applications*, Vol. 3401. Springer, Berlin, Heidelberg, pp. 456–462, URL: https://doi.org/10.1007/978-3-540-31852-1_55.
- Rabin, Y., Shitzer, A., 1995. Exact solution to the one-dimensional inverse-Stefan problem in nonideal biological tissues. *J. Heat Transfer* 117 (2), 425–431, URL: <https://doi.org/10.1115/1.2822539>.
- Rabin, Y., Shitzer, A., 1997. Combined solution of the inverse Stefan problem for successive freezing/thawing in nonideal biological tissues. *J. Biomech. Eng.* 119 (2), 146–152, URL: <https://doi.org/10.1115/1.2796073>.
- Rubinsky, B., Shitzer, A., 1976. Analysis of a Stefan-like problem in a biological tissue around a cryosurgical probe. *J. Heat Transfer* 98 (3), 514–519, URL: <https://doi.org/10.1115/1.3450587>.
- Sartoretto, F., Spigler, R., 1990. Numerical solution for the one-phase Stefan problem by piecewise constant approximation of the interface. *Computing* 45, 235–249, URL: <https://doi.org/10.1007/BF02250635>.
- Savović, S., Caldwell, J., 2009. Numerical solution of Stefan problem with time-dependent boundary conditions by variable space grid method. *Therm. Sci.* 13 (4), 165–174, URL: <https://doi.org/10.2298/TSCI0904165S>.
- Schiesser, W., 1991. *The Numerical Method of Lines: Integration of Partial Differential Equations*. Academic Press, San Diego.
- Tao, L.N., 1979. The Stefan problem of a polymorphous material. *J. Appl. Mech.* 46 (4), 789–794, URL: <https://doi.org/10.1115/1.3424655>.
- Tarantino, R., Szigeti, F., Colina-Morles, E., 2000. Generalized Luenberger observer-based fault-detection filter design: an industrial application. *Control Eng. Pract.* 8, 665–671, URL: [https://doi.org/10.1016/S0967-0661\(99\)00181-1](https://doi.org/10.1016/S0967-0661(99)00181-1).
- Uhlig, M., Ezquer, F., Ezquer, M., 2022. Improving cell recovery: Freezing and thawing optimization of induced pluripotent stem cells. *Cells* 11 (5), 799, URL: <https://doi.org/10.3390/cells11050799>.
- Šarler, B., 1995. Stefan's work on solid-liquid phase changes. *Eng. Anal. Bound. Elem.* 16 (2), 83–92, URL: [https://doi.org/10.1016/0955-7997\(95\)00047-X](https://doi.org/10.1016/0955-7997(95)00047-X).
- Vries, D., Keesman, K.J., Zwart, H., 2007. A Luenberger observer for an infinite dimensional bilinear systems: A UV disinfection example. *IFAC Proc. Vol.* 40 (20), 667–672, URL: <https://doi.org/10.3182/20071017-3-BR-2923.00109>.
- Wang, W., Gao, Z., 2003. A comparison study of advanced state observer design techniques. In: *Proceedings of the American Control Conference*, Vol. 6. pp. 4754–4759, URL: <https://doi.org/10.1109/ACC.2003.1242474>.